

1 Estimation of raindrop size distribution and rain rate with infrared 2 surveillance camera in dark conditions

3 Jinwook Lee¹, Jongyun Byun¹, Jongjin Baik¹, Changhyun Jun¹, Hyeon-Joon Kim¹

4 ¹Department of Civil and Environmental Engineering, College of Engineering, Chung-Ang University-example, Seoul, 06974,
5 South Korea

6 Correspondence to: Hyeon-Joon Kim (hjkim22@cau.ac.kr)

7 **Abstract.** This study estimated raindrop size distribution (DSD) and rainfall intensity with an infrared surveillance camera in
8 dark conditions. Accordingly, rain streaks were extracted using a k -nearest neighbor (KNN)-based algorithm. The rainfall
9 intensity was estimated using DSD based on physical optics analysis. The estimated DSD was verified using a disdrometer.
10 ~~Furthermore, a tipping-bucket rain gauge was used for comparison, for the two rainfall events.~~ The results are summarized as
11 follows. First, a KNN-based algorithm can accurately recognize rain streaks from complex backgrounds captured by the
12 camera. Second, the number concentration of raindrops obtained through closed-circuit television (CCTV) images ~~was similar~~
13 ~~to had values between $100 \text{ mm}^{-1}\text{m}^{-3}$ and $1,000 \text{ mm}^{-1}\text{m}^{-3}$, the actual Particle Size RMSE for the number concentration by CCTV~~
14 ~~and Particle Size and VELOCITY (PARSIVEL)-observed number concentration) was $72.3 \text{ mm}^{-1}\text{m}^{-3}$ and $131.6 \text{ mm}^{-1}\text{m}^{-3}$ in the~~
15 0.5 to 1.5 mm section. Third, maximum raindrop diameter and the number concentration of 1 mm or less produced similar
16 results during the period with a high ratio of diameters of 3 mm or less. Finally, after comparing with the 15-min cumulative
17 PARSIVEL rain rate, the mean absolute percent error (MAPE) was 44%. ~~The 49% and 23%, respectively. In addition, the~~
18 differences according to rain rate can be ~~determined. The found that the MAPE was 3236% at a rain rate of less than 2 mm h^{-1}~~
19 ~~and 7380% at a rate above 2 mm h^{-1} . Also, when the rain rate was greater than 5 mm h^{-1} , MAPE was 33%.~~ We confirmed the
20 possibility of estimating an image-based DSD and rain rate obtained based on low-cost equipment during dark conditions.

21 1 Introduction

22 Precipitation data is vital in water resource management, hydrological research, and global change analysis. The primary means
23 of measuring precipitation is to use a rain gauge (Allamano et al., 2015) to collect raindrops from the ground. Due to the
24 restrictions on the installation environment of the rain gauge, it is difficult to understand the spatial rainfall distribution in
25 mountains and urban areas (Kidd et al., 2017). Furthermore, the tipping-bucket-type rain gauge, which accounts for most rain
26 gauges, has a discrete observation resolution (0.1 or 0.5 mm) for the discrete time-steps, producing uncertainty in temporal
27 rainfall variation. ~~For this reason, weighing gauges are nowadays used very often instead of tipping-bucket-type. the weighing~~
28 ~~gauge is a meteorological instrument used to observe and analyze various precipitation, including rainfall and snowfall. Also,~~
29 ~~the tipping bucket has a large error due to the observation time delay when the rainfall is less than 10 mm h^{-1} compared to the~~

서식 있음: 글꼴 색: 자동

서식 있음: 글꼴 색: 자동

서식 있음: 글꼴 색: 자동

서식 있음: 글꼴 색: 자동

서식 있음: 위 첨자

서식 있음: 글꼴 색: 자동

서식 있음: 글꼴 색: 자동

서식 있음: 글꼴 색: 자동

서식 있음: 글꼴 색: 자동

서식 있음: 글꼴 색: 자동

서식 있음: 글꼴 색: 자동

서식 있음: 글꼴 색: 자동

30 weighing gauge. However, when the observation time size is set to 10 to 15 minutes, the relative percentage error has a very
31 low value of -6.7~2.5%, resulting in high accuracy (Colli et al., 2014).

32 In contrast, it is possible to obtain spatial rainfall information on a global scale with remote sensing techniques (Famiglietti
33 et al., 2015). However, remote sensing techniques provide only indirect measurements that must be continuously calibrated
34 and verified through ground-level precipitation measurements (Michaelides et al., 2009). Recently, a disdrometer capable of
35 investigating the microphysics characteristics of rainfall has been used for observation instead of the traditional rainfall
36 observation instrument (Kathiravelu et al., 2016). However, these devices cannot be widely installed because of their high cost
37 and difficulty in accessing observational data. Consequently, a high-resolution and low-cost ground precipitation monitoring
38 network has not yet been established.

39 With the advent of the Internet of Things (IoT) era, using non-traditional sources is attractive for improving the spatio-
40 temporal scale of existing observation networks (McCabe et al., 2017). In recent years, such cases have been common in
41 rainfall observation. For example, there have been attempts to estimate rainfall using sensors to capture signal attenuation
42 characteristics in commercial cellular communication networks (Overeem et al., 2016), vehicle wipers (Raibei et al., 2013),
43 and smartphones (Guo et al., 2019). Furthermore, crowdsourcing information has been used to confirm the utility of estimating
44 regional rainfall (Haberlandt and Sester, 2010; Rabiei et al., 2016; Yang and Ng, 2017).

45 In a similar context, a surveillance camera is a sensor with high potential. Surveillance cameras are often referred to as
46 closed-circuit television (CCTV). Compared with other crowdsourcing methods, the visualization data of surveillance cameras
47 are highly intuitive (Guo et al., 2017). Therefore, they have been used in various fields (Cai et al., 2017; Nottle et al., 2017;
48 Hua, 2018). In Korea, public surveillance camera installations have been rapidly increasing, from approximately 150,000 in
49 2008 to 1.34 million in 2020—approximately a public CCTV camera per 0.07 km². Thus, the potential for precipitation
50 estimation using camera sensing is expected to be greater in Korea.

51 Recently, various studies have been conducted to estimate rainfall intensity using the rain streak image obtained from
52 surveillance camera videos. Many studies attempted to use artificial intelligence to capture changes in the image captured by
53 the camera when it rains (Zen et al., 2019; Avanzato and Beritelli, 2020; Wang et al., 2022). In contrast, some studies have
54 tried to estimate rainfall intensity using geometrical optics and photographic analyses. Typically, the rain streak layer is
55 separated from the raw image or video. A rain streak is the visual appearance of raindrops caused by visual persistence—
56 raindrops falling because of the blur phenomenon of raindrop movement from the camera's exposure time appears as streaks
57 on the image. Garg and Nayar (2005) made one of the first attempts to measure this rainfall.

58 It is true that these previous studies confirmed the possibility of rainfall measurement using surveillance cameras. However,
59 several limitations still prevent the actual expansion of the measurement systems using surveillance cameras. In general, most
60 surveillance cameras are installed for monitoring purposes, and people's faces are inevitably captured. Therefore, it is not easy
61 to disclose the data due to privacy concerns. Data storage and transmission are also limitations. Since most surveillance
62 cameras use a hard disk, data must be taken out directly. In other words, rainfall estimation cannot be done in real-time unless
63 a system is in place to transmit data over the Internet. In addition, the applicability to night-time is more limited. In the case of

64 general surveillance cameras in the past, observation is possible only when sunlight exists. For the observation system to
65 expand, these various limitations must be addressed, and it seems that a lot of time and effort are needed. Nevertheless, research
66 to develop algorithms using surveillance cameras in various conditions and to confirm applicability can have sufficient
67 meaning. The case of dark conditions is one of the conditions worth studying. This is because the recently installed surveillance
68 cameras are equipped with an Infrared recording function, so most cameras will be able to take videos at night soon. However,
69 the final purpose of utilizing these devices and the method is not to replace existing devices. It could be a supplement to
70 improve the spatiotemporal resolution and accuracy of existing observation instruments. In particular, a study on the drop size
71 distribution of rainfall, rather than simple rainfall estimation, would have more potential application value.

72 Since then, many studies have been conducted to develop and improve efficient algorithms. Allamano et al. (2015)
73 proposed a framework to estimate the quantitative rainfall intensity using camera images based on physical optics from a
74 hydrological perspective. Dong et al. (2017) proposed a more robust approach to identifying raindrops and estimating rainfall
75 using a grayscale function, making grayscale subtraction nonlinear. Jiang et al. (2019) proposed an algorithm that decomposes
76 rain-containing images into rain streak layers and rainless background layers using convex optimization algorithms and
77 estimates instantaneous rainfall intensity through geometric optical analysis.

78 Some studies (e.g., Dong et al., 2017) have sought to estimate raindrop size distribution (DSD) using a surveillance camera.
79 However, neither existing studies have focused on the time when video can be captured with visible light. It is impossible to
80 obtain input data without visible light using the existing image-based rainfall measurement method. Thus, these methodologies
81 are only applicable in daytime conditions. However, when recording using infrared rays, it is possible to obtain a rainfall image
82 even when there is no sunlight. No study has estimated the rain in dark conditions to our knowledge. Furthermore, most
83 previous studies did not verify the estimated DSD using a disdrometer. In contrast, this study estimated DSD with an infrared
84 surveillance camera in dark conditions, based on which rainfall intensity was also estimated. Rain streaks were extracted using
85 a k-nearest neighbor (KNN)-based algorithm. The DSD was used to calculate rainfall intensity with physical optics analysis
86 and verified using a PARticle Size and VELOCITY (PARSIVEL) disdrometer. (Löffler-Mang and Joss, 2000).

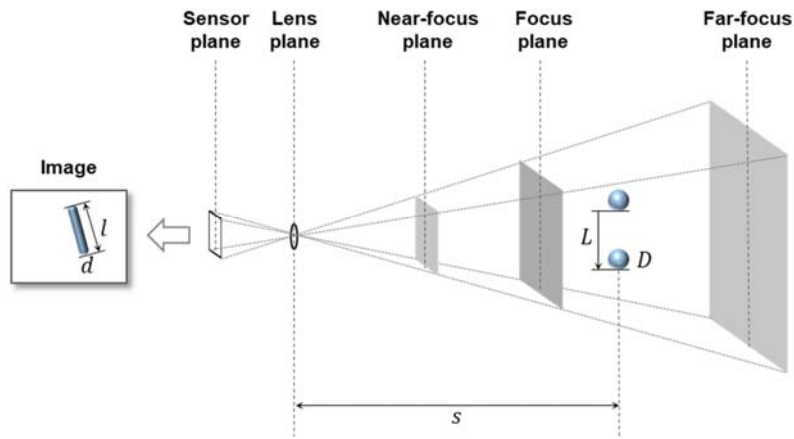
87 **2 Methodology**

88 **2.1 Recording video containing rain streaks using infrared surveillance camera**

89 The surveillance camera records video. The video looks continuous, but it is also composed of discrete still images, so-called
90 frames. The frequency of recording frames (i.e., acquisition rate) is called frames per second (fps). In other words, fps is how
91 many images are taken per second for recording video. Another important factor in video recording is exposure time. Exposure
92 time, also called shutter speed, refers to the time the camera sensor is exposed to light to capture a single frame. The real
93 raindrops are close to a circle, but in a single image, the raindrops look like a streak. This is because raindrops move at a high
94 speed during the exposure time. Therefore, the raindrops that moved during the exposure time are visualized in the rain streaks
95 in a single frame.

96 Fig. 1 shows an example of capturing a raindrop for a single frame. Here, only the raindrops near the point of focus are
 97 visible, and objects that are more than a certain distance appear invisible. That is, the point where the focus is best is called the
 98 focus plane, and there is a range in which it can be recognized that objects are focused before and after the focus plane. The
 99 closest plane that can be considered to be in focus is called the near-focus plane, and the farthest plane is called the far-focus
 100 plane. This range is generally called depth of field (DoF). Ultimately, the rainfall intensity can be estimated based on the
 101 volume and raindrops in the DoF.

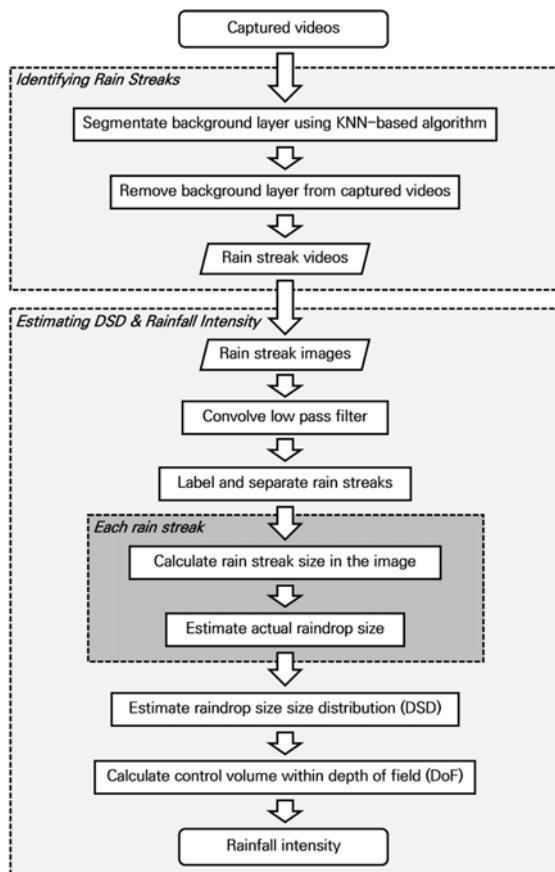
102 In this study, an infrared surveillance camera was considered under dark conditions. Here, the dark condition refers to a
 103 condition in which raindrops cannot be captured by a general surveillance camera with visible light. Infrared cameras emit
 104 near-infrared rays through an infrared emitter and receive the reflected light from the objects. Accordingly, it has the advantage
 105 of being able to detect raindrops that are invisible to the human eye.



106 Figure 1: Schematic diagram of the photographed rain streak in the image and the movement of a raindrop during the exposure
 107 time.

108 2.2 Algorithm for identifying rain streaks and estimating DSD and rain rate

109 Image-based rainfall estimation can be divided into two processes: identifying rainfall streaks and estimating DSD. Fig. 42
 110 illustrates these processes in a flowchart. Identifying rain streaks requires an algorithm that separates the moving rain streaks
 111 from the background layer, ~~as explained in Section 2.1.~~ Next, in estimating DSD, raindrops are extracted from the image of
 112 the rain streaks, and the overall distribution is obtained. ~~This process is explained in Section 2.2.~~



113 **Figure 12.** Flowchart of the methodology for estimating DSD and rainfall intensity.

114 **2.1 Algorithm for identifying rain streaks**

115 Most existing algorithms aim to remove raindrops in images because raindrops are considered noise in object detection
 116 and tracking (Duthon et al., 2018). Such algorithms are categorized into multiple-image-based and single-image-based
 117 approaches (Jiang et al., 2018).

← 서식 있음: 표준

← 서식 있음: 들여쓰기: 첫 줄: 1.42 글자

118 For example, Garg and Nayar (2007) classified the conditions in which the brightness difference between the previous
 119 pixel and that of the next pixel exceeds a specific threshold over time, assuming that the background is fixed. Improved
 120 algorithms were then developed considering the temporal correlation of raindrops (Kim et al., 2015) and chromatic properties
 121 (Santhaseelan and Asari, 2015). Tripathi and Mukhopadhyay (2014) proposed a framework that removes rain that reduces the
 122 visibility of the scene to improve the detection performance of image feature information. However, single-image-based
 123 algorithms rely more on the properties of raindrops (Deng et al., 2018). The central idea of a single-image-based algorithm is
 124 to decompose rain-containing images into rainless layers (Li et al., 2016; Deng et al., 2018; Jiang et al., 2018).

125 An image including grayscale rainfall may be mathematically expressed in a two-dimensional (2D) matrix in which each
 126 element has a grayscale value. A single image ($m \times n$) is expressed as follows (Jiang et al., 2018):

$$127 \quad O = B + R, \tag{1}$$

128 where $O \in R^{m \times n}$, $B \in R^{m \times n}$, and $R \in R^{m \times n}$ are the raw image, rain-free background layer, and rain streak layer.
 129 Accordingly, various algorithms are available for rain streak identification. Different still image and video-based algorithms
 130 have been proposed to eliminate objects such as moving objects for application to actual surveillance cameras. However, most
 131 of these algorithms face optimization problems because of the vast number of decision variables (Jiang et al., 2019). This task
 132 is not easy to solve or requires excessive computation time. Therefore, existing studies present techniques suitable for post-
 133 analysis rather than application in real-time. The use of complex algorithms can increase versatility and accuracy, but there is
 134 a trade-off that reduces computational speed. The time required for such computing is a critical disadvantage in practical
 135 applications for estimating rainfall intensity.

136 In this study, a KNN-based segmentation algorithm (Zivkovic and Heijden, 2006), a popular non-parametrical method for
 137 background subtraction, was considered for segmenting the rain streaks (foreground) and background layers. KNN is used in
 138 classification and regression problems (Bouwman et al., 2010). The concept of KNN is that similar things are close—the
 139 KNN-based segmentation algorithm finds the closest k samples (neighbors) to the unknown sample using Euclidean distance
 140 to determine the class (i.e., foreground or background). Thus, the KNN-based segmentation method to detect foreground
 141 changes in the video was used to identify rain streaks by recording infrared videos under conditions with little background
 142 influence. In the algorithm, The KNN subtractor works by updating the parameters of a Gaussian mixture model for more
 143 accurate kernel density estimation (Trnovský et al., 2017). KNN is more efficient for local density estimation (Qasim et al.,
 144 2021); therefore, the algorithm is highly efficient if the number of foreground pixels is low.

145 We used the package provided by OpenCV to implement the KNN-based segmentation algorithm (Zivkovic and Heijden,
 146 2006). Accordingly, three main parameters (history, dist2Threshold, detectShadows) needed to be set. Table 1 presents the
 147 description of the parameters used for the KNN background subtractor package.

148 **Table 1.** Parameters in KNN background subtractor package in OpenCV.

Parameter	Description
-----------	-------------

history	Length of the history
dist2Threshold	Threshold on the squared distance between the pixel and the sample to decide whether a pixel is close to that sample. This parameter does not affect the background update.
detectShadows	If true, the algorithm will detect shadows and mark them. This decreases the speed slightly, so if you do not need this feature, set the parameter to false.

149 **2.2 Estimation of DSD and rain rate**

150 It is essential to capture raindrops within the camera's depth of field (DoF) to calculate the final DSD and rainfall intensity. ←
 151 Accordingly, this study proposed a novel algorithm to extract each rain streak from the rain streaks image. First, we applied a
 152 low-pass filter to the rain streaks image to remove unfocused raindrops that may remain in the image, which smooths each
 153 pixel using a 2D kernel. **Videos from infrared mode have usually a blur effect. Thus, the additional 2D kernel was applied to**
 154 **remove the pixels having blur.** Highly detailed parts (e.g., out-of-focus raindrops and some noises) are erased, leaving some
 155 clear rain streaks. A background layer with a value of 0 and a part not in the image were separated to extract the rain streaks
 156 and labeled one by one to identify each rain streak from the image.

157 Because the rain streak observed in the surveillance camera image causes an angle difference (influenced by the wind), a
 158 diameter estimation process considering the angle of the rain streak (fall angle of a raindrop) is required. If the angle of rain
 159 streak is considered and converted to the raindrop diameter through the horizontal pixel size in the image, the shape change in
 160 the raindrop because of air buoyancy (i.e., during the falling of the raindrop) may not be reflected, and overestimation can
 161 occur.

162 Accordingly, the representative angle of each extracted rain streak was calculated. The border information of each rain
 163 streak was obtained, and center axis information of the rain streak was obtained based on the border information to calculate
 164 the drop angle. Moreover, the rain streak was rotated to set the long and short axes of the streak at 0° and 90°, using the angle
 165 information.

166 The size of raindrops in the rain streaks image can be estimated through the analysis of microphysical characteristics of
 167 raindrop and geometric optical analysis (Keating, 2002). The instantaneous velocity of a raindrop on the ground can be
 168 estimated from the exposure time and the size of the raindrop. However, the distance from the raindrop to the lens surface (i.e.,
 169 the object distance) is unknown and should be inferred. Object distance can be calculated through physical optics analysis
 170 because it causes perspective distortion. Assuming a raindrop is spherical, the length of the trajectory where the raindrop falls
 171 when the camera is exposed and the diameter of the raindrop can be inferred through the lens equation (Keating, 2002):

172
$$L(s) = \frac{d_f - f}{d_f} \frac{h_s}{h_p} l_p s, \quad (2)$$

173
$$D(s) = \frac{d_f - f}{d_f} \frac{w_s}{w_p} d_p s, \quad (3)$$

서식 있음: 들여쓰기: 첫 줄: 1.42 글자

174 where s is the distance from the raindrop to the lens plane (mm). $L(s)$ and $D(s)$ are the length of falling trajectory during camera
 175 exposure (rain streak) and the raindrop's diameter. d_f is the focus distance (mm), f is focal length (mm). h_s and w_s are the
 176 vertical and horizontal sizes of the active area of the image sensor (mm), and h_p and w_p are the vertical and horizontal sizes of
 177 the captured image (in number of pixels). l_p and d_p are the length and width of the rain streaks in the image (in number of
 178 pixels).

179 It is then possible to infer the falling speed of raindrops using the camera's exposure time (Jiang et al., 2019), as follows:

$$180 \quad v(s) = \frac{L(s)}{1000\tau}, \quad (4)$$

181 where τ is the exposure time of the camera (seconds) and $v(s)$ is the fall velocity of the raindrop from the image. Furthermore,
 182 the fall velocity of a raindrop can be approximated by an empirical formula for raindrop diameter. The most frequently used
 183 equation is as follows (Atlas et al., 1973; Friedrich et al., 2013):

$$184 \quad v(D) = 9.65 - 10.3\exp(-0.6D), \quad (5)$$

185 where D is the raindrop diameter and v is the fall velocity of raindrop. The actual diameter of raindrops can be obtained by
 186 solving the equation with the fall velocity obtained through the exposure time and Eqs. (4) and (5). Furthermore, the DoF for
 187 the images using the camera's setting information can be calculated, and the effective volume for estimating rainfall intensity
 188 can be obtained. Details of the process are described in previous studies (Allamano et al., 2015; Jiang et al., 2019).

189 The control volume must be determined to estimate the rainfall intensity using the diameter of each raindrop. An understanding
 190 of DoF is required to achieve the volume. The DoF, is simply the range at which the camera can accurately focus and capture
 191 the raindrops. Calculating this range requires obtaining the near and far focus planes as follows:

$$192 \quad s_n = \frac{d_f \cdot f^2}{f^2 + N \cdot c_p \cdot (d_f - f)}, \quad (6)$$

$$193 \quad s_f = \frac{d_f \cdot f^2}{f^2 - N \cdot c_p \cdot (d_f - f)}, \quad (7)$$

194 where s_n and s_f are the distances from the near and far focus planes. c_p is the maximum permissible circle of confusion, a
 195 constant determined by the camera manufacturers. N is the F-number of the lens relevant to the aperture diameter. Accordingly,
 196 the theoretical sampling volume (V , m³) indicate the truncated rectangular pyramid between the near and far focus planes:

$$197 \quad V = \frac{1}{3 \cdot 10^9} \left(\frac{d_f - f}{d_f \cdot f} \right)^2 w_s h_s (s_f^3 - s_n^3), \quad (8)$$

198

199 Then, we used the gamma distribution equation, Eq. (6), proposed by Ulbrich (1983), to calculate DSD parameters using
 200 data at every 1 min interval.

$$201 \quad N(D) = N_0 D^\mu \exp(-\lambda D), \quad (9)$$

202 where $N(D)$ ($\text{mm}^{-1}\text{m}^{-3}$) is the number concentration value per unit volume for each size channel, and N_0 ($\text{mm}^{-1-\mu}\text{m}^{-3}$) is an
 203 intercept parameter representing the number concentration when the diameter has 0 value. D (mm) and A (mm^{-1}) are the drop
 204 diameter (mm) and slope parameter. Raindrops smaller than 8.0 mm were used to avoid considering non-weather data such as
 205 leaps and bugs (Friedrich et al., 2013).

206 The gamma distribution relationship is a function of formulating the number concentration per unit diameter and unit
 207 volume. It was proposed by Marshall and Palmer (1948) as improved model of exponential distribution as a favorable form to
 208 reflect various rainfall characteristics. By including the term containing μ in the distribution function, the shape of the number
 209 concentration distribution for small drops smaller than 1 mm is improved.

$$210 \quad N(D) = N_0 \exp(-AD), \quad (10)$$

211 As the A decreases, the slope of the distribution shape decreases and the proportion of large drop increases. Conversely, as
 212 the value increases, the distribution slope becomes steeper, and the weight of the large particles decreases. When μ has a large
 213 value, the distribution is convex upward, and it has a distribution with a sharp decrease in number concentration at small
 214 diameters. Whereas when it has a negative value, the distribution is convex downward with an increase in the concentration
 215 of drops smaller than 1 mm. In the gamma distribution, the μ is mainly affected by the difference in concentration of raindrops
 216 smaller than 3 mm (Vivekanandan et al., 2004).

217 Vivekanandan et al. (2004) explained the reason for using the gamma distribution as follows. First, it is sufficient to
 218 calculate the rainfall estimation equation using only the first, third, and fourth moments (Eq. (11)) (Smith, 2003). Second, the
 219 long-term raindrop size distribution has an exponential distribution shape (Yuter and Houze, 1997).

220 The raindrop size distribution observed from the ground is the result of the microphysical development of raindrops falling
 221 from precipitation clouds. The drop size distribution shape is changed during fall by microphysical processes such as collision,
 222 merging, and evaporation, and changes in the concentration of drops larger than 7.5 mm and small drops occur mainly. As a
 223 result, the drop size distribution observed on the ground mainly follows the gamma distribution shape (Ulbrich, 1983; Tokay
 224 and Short, 1996). The gamma distribution relationship should be used to analyze the distribution of raindrops that are actually
 225 floating and falling.

$$226 \quad M_n = \int_{D_{min}}^{D_{max}} D^n N(D) dD, \quad (11)$$

227 Eq. (11) indicate a moment expression for the n^{th} order. For example, the second moment is calculated as the product of
 228 the square of the diameter of each channel and the number concentration and the diameter of each channel. Each moment value
 229 has a different microphysical meaning. Therefore, the gamma distribution including three dependent parameters is more
 230 advantageous in reflecting the microphysical characteristics of the precipitation system than the exponential distribution
 231 including two dependent parameters. Eq. (11) can be expressed in gamma distribution format as follows:

$$232 \quad M_n = \int_{D_{min}}^{D_{max}} D^n N(D) dD = N_0 A^{-(\mu+n+1)} \Gamma(\mu + n + 1), \quad (12)$$

233 where N_T (total number concentration, m^{-3}) is the zero-order moment (M_0) and represents the total number concentration of
 234 raindrops per unit volume. η was determined for calculating μ and Λ . In this study, a combination of moments in the ratio of
 235 M_2 , M_4 , and M_6 , which accurately represents the characteristics of small rainfall particles, was applied (Vivekanandan et al.,
 236 2004):

$$237 \quad \eta = \frac{(M_2)^2}{(M_2)(M_6)} = \frac{(\mu+3)(\mu+4)}{(\mu+5)(\mu+6)}, \quad (13)$$

238 μ and Λ are calculated as follows:

$$239 \quad \mu = \frac{(7-11\eta)-[(7-11\eta)^2-4(\eta-1)(30\eta-12)]^{1/2}}{2(\eta-1)}, \quad (14)$$

$$240 \quad \Lambda = \left[\frac{M_2 \Gamma(\mu+5)}{M_4 \Gamma(\mu+3)} \right]^{1/2} = \left[\frac{M_2(\mu+4)(\mu+3)}{M_4} \right]^{1/2}, \quad (15)$$

241 A larger value of D_m (mm) estimated using Eq. (16), the diameter of the average mass of raindrops contained in the unit
 242 volume, indicates that predominantly larger drops are distributed.

$$243 \quad D_m = \frac{M_4}{M_3}, \quad (16)$$

244 R ($mm \ h^{-1}$) is the rain rate calculated using Eq. (17).

$$245 \quad R = \frac{6\pi}{10^4} \int_{D_{min}}^{D_{max}} D^3 N(D) V(D) dD, \quad (17)$$

246 3 Study site and observation equipment

247 This study used a building's rooftop as the study site. The building is the Chung-Ang University's Bobst Hall, located in the
 248 central region of Seoul in Korea. It is located at $37^\circ 30' 13''$ north latitude and $126^\circ 57' 27''$ east longitude, at an elevation of
 249 42 m. Fig. 23 illustrates the CCTV (marked with a red circle) and PARSIVEL installed at the study point. The CCTV was
 250 used for the main analysis, and PARSIVEL was considered for verification purposes.



(a) Surveillance camera



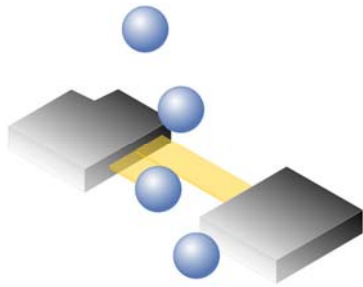
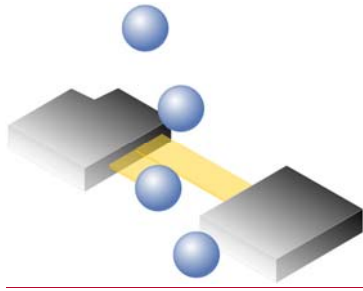
(b) PARSIVEL

251 **Figure 23:** Observation measurements considered in this study.

252 The CCTV model used in this study is DC-T333CHRX, developed by IDIS. The camera has a 1/1.7 inch complementary
 253 metal-oxide semiconductor (CMOS) with a height and width of 5.70 mm and 7.60 mm. The focal length is 4.5 mm, and the
 254 F-number of the lens is 1.6. The shutter speed was set to 1/250 s, and the frame per second (fps) was set to 30. The infrared
 255 ray distance is 50 m. The maximum permissible circle of confusion is 0.005 mm. The camera's resolution is 1,080 pixels for
 256 the height and 1,920 pixels for the width, but the cropped images (640×640 pixels) were considered for the analysis.

257 The PARSIVEL is a ground meteorological instrument that can observe precipitation particles' diameter and fall speed
 258 (e.g., raindrops, snow particles, hail) (Löffler-Mang and Joss, 2000). The meteorological information, including raindrop
 259 size, is used to estimate the quantitative precipitation amount and reveal the precipitation system's microphysical
 260 characteristics and development mechanism.

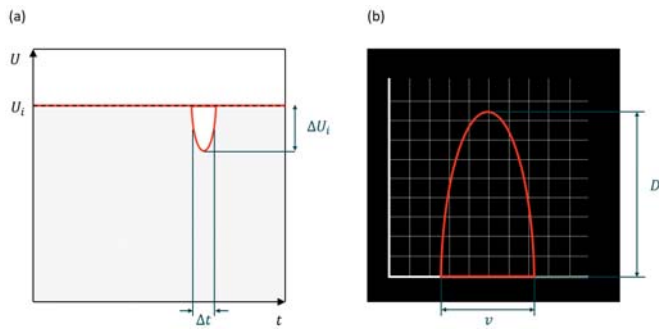
261 The PARSIVEL used in this study is the second version of the instrument manufactured by OTT in Germany, and it is
 262 improved observation accuracy of small particles. The PARSIVEL uses a laser-based optical sensor to send a laser from the
 263 transmitter and continuously receive it from the receiver (Fig. 34). As the laser beam moves from the transmitter to the receiver,
 264 the precipitation particle passes over the laser beam, and the size and velocity of the precipitation particle are observed (Nemeth
 265 and Hahn, 2005). The diameter and velocity of the particle are calculated by calculating the time the particle passes through
 266 the laser and the laser intensity that decreases during the passage (Fig. 45).



267

268

269 **Figure 34.** Functional principle of the PARSIVEL disdrometer.



270

271 **Figure 45.** (a) Signal changes whenever a particle falls through the beam anywhere within the measurement area. (b) The degree of
 272 dimming is a measure of the particle's size; together with the duration of the signal, the fall velocity can be derived.

273 Parameters such as rain rate, reflectivity, and momentum of raindrops are calculated through particle concentration values
 274 for each diameter and falling speed channel obtained through PARSIVEL observation. In this study, the temporal resolution
 275 of the observation data was set to 1 minute. The particle diameters from 0.2 to 25 mm (Table 21 in Appendix) and fall velocity
 276 from 0.2 to 20 m s⁻¹ (Table 32 in Appendix) can be observed by the PARSIVEL. The particle diameter and the fall speed each
 277 have 32 observation channels, so the number of observed particles for the time resolution set in 1,024 channels (32×32) is
 278 observed. The first and second channels of diameter are not included in the observable range of the PARSIVEL and are treated
 279 as noise. Therefore, the observation data of the first and second diameter channels were not considered in the actual analysis.
 280 The detailed information on the specifications of the PARSIVEL is presented in Table 42.

283 **Table 2: The representative diameter and spread for each diameter channel class.**

Class number	Class average (mm)	Class spread (mm)	Class number	Class average (mm)	Class spread in (mm)
1	0.062	0.125	17	3.250	0.500
2	0.187	0.125	18	3.750	0.500
3	0.312	0.125	19	4.250	0.500
4	0.437	0.125	20	4.750	0.500
5	0.562	0.125	21	5.500	1.000
6	0.687	0.125	22	6.500	1.000
7	0.812	0.125	23	7.500	1.000
8	0.937	0.125	24	8.500	1.000
9	1.062	0.125	25	9.500	1.000
10	1.187	0.125	26	11.000	2.000
11	1.375	0.250	27	13.000	2.000
12	1.625	0.250	28	15.000	2.000
13	1.875	0.250	29	17.000	2.000
14	2.125	0.250	30	19.000	2.000
15	2.375	0.250	31	21.500	3.000
16	2.750	0.500	32	24.500	3.000

286 **Table 3: The representative fall velocity and spread for each diameter channel class.**

Class number	Class average (m s ⁻¹)	Class spread (m s ⁻¹)	Class number	Class average (m s ⁻¹)	Class spread (m s ⁻¹)
1	0.050	0.100	17	2.600	0.400
2	0.150	0.100	18	3.000	0.400

- 서식 있음:** 들어쓰기: 첫 줄: 1.42 글자, 줄 간격: 1.5줄
- 서식 있음:** 위치: 가로: 왼쪽, 기준: 세로 막대형, 세로: 기본, 기준: 여백, 가로: 0 글자, 텍스트 배치: 둘러싸기
- 서식 있음:** 위치: 가로: 왼쪽, 기준: 세로 막대형, 세로: 기본, 기준: 여백, 가로: 0 글자, 텍스트 배치: 둘러싸기
- 서식 있음:** 위치: 가로: 왼쪽, 기준: 세로 막대형, 세로: 기본, 기준: 여백, 가로: 0 글자, 텍스트 배치: 둘러싸기
- 서식 있음:** 위치: 가로: 왼쪽, 기준: 세로 막대형, 세로: 기본, 기준: 여백, 가로: 0 글자, 텍스트 배치: 둘러싸기
- 서식 있음:** 위치: 가로: 왼쪽, 기준: 세로 막대형, 세로: 기본, 기준: 여백, 가로: 0 글자, 텍스트 배치: 둘러싸기
- 서식 있음:** 위치: 가로: 왼쪽, 기준: 세로 막대형, 세로: 기본, 기준: 여백, 가로: 0 글자, 텍스트 배치: 둘러싸기
- 서식 있음:** 위치: 가로: 왼쪽, 기준: 세로 막대형, 세로: 기본, 기준: 여백, 가로: 0 글자, 텍스트 배치: 둘러싸기
- 서식 있음:** 위치: 가로: 왼쪽, 기준: 세로 막대형, 세로: 기본, 기준: 여백, 가로: 0 글자, 텍스트 배치: 둘러싸기
- 서식 있음:** 위치: 가로: 왼쪽, 기준: 세로 막대형, 세로: 기본, 기준: 여백, 가로: 0 글자, 텍스트 배치: 둘러싸기
- 서식 있음:** 위치: 가로: 왼쪽, 기준: 세로 막대형, 세로: 기본, 기준: 여백, 가로: 0 글자, 텍스트 배치: 둘러싸기
- 서식 있음:** 위치: 가로: 왼쪽, 기준: 세로 막대형, 세로: 기본, 기준: 여백, 가로: 0 글자, 텍스트 배치: 둘러싸기
- 서식 있음:** 위치: 가로: 왼쪽, 기준: 세로 막대형, 세로: 기본, 기준: 여백, 가로: 0 글자, 텍스트 배치: 둘러싸기
- 서식 있음:** 위치: 가로: 왼쪽, 기준: 세로 막대형, 세로: 기본, 기준: 여백, 가로: 0 글자, 텍스트 배치: 둘러싸기
- 서식 있음:** 위치: 가로: 왼쪽, 기준: 세로 막대형, 세로: 기본, 기준: 여백, 가로: 0 글자, 텍스트 배치: 둘러싸기
- 서식 있음:** 위치: 가로: 왼쪽, 기준: 세로 막대형, 세로: 기본, 기준: 여백, 가로: 0 글자, 텍스트 배치: 둘러싸기
- 서식 있음:** 위치: 가로: 왼쪽, 기준: 세로 막대형, 세로: 기본, 기준: 여백, 가로: 0 글자, 텍스트 배치: 둘러싸기
- 서식 있음:** 위치: 가로: 왼쪽, 기준: 세로 막대형, 세로: 기본, 기준: 여백, 가로: 0 글자, 텍스트 배치: 둘러싸기
- 서식 있음:** 위치: 가로: 왼쪽, 기준: 세로 막대형, 세로: 기본, 기준: 여백, 가로: 0 글자, 텍스트 배치: 둘러싸기
- 서식 있음:** 위치: 가로: 왼쪽, 기준: 세로 막대형, 세로: 기본, 기준: 여백, 가로: 0 글자, 텍스트 배치: 둘러싸기

2	0.250	0.100	19	3.400	0.400
4	0.350	0.100	20	3.800	0.400
5	0.450	0.100	21	4.400	0.800
6	0.550	0.100	22	5.200	0.800
7	0.650	0.100	23	6.000	0.800
8	0.750	0.100	24	6.800	0.800
9	0.850	0.100	25	7.600	0.800
10	0.950	0.100	26	8.400	1.600
11	1.100	0.200	27	10.400	1.600
12	1.300	0.200	28	12.000	1.600
13	1.500	0.200	29	13.600	1.600
14	1.700	0.200	30	15.200	1.600
15	1.900	0.200	31	17.600	3.200
16	2.200	0.400	32	20.800	3.200

287

288 Table 24: Technical information of the PARSIVEL disdrometer.

Items		Technical information	Technical specifications
Wavelength of optical sensor		780 nm	
Measuring area		30 × 180 mm (54 cm ²)	
Measuring range	Size	0.2 ~ 25 mm (32 channel class)	
	Fall velocity	0.2 ~ 20 m s ⁻¹ (32 channel class)	
Precipitation intensity		0.001 ~ 1,200 mm h ⁻¹	
Measurement time interval		10 sec ~ 60 min	
Instrument dimensions (H×W×D)		670 × 600 × 114 mm	

289

290 4 Application result

291 4.1 Rainfall event

292 We considered atwo rainfall eventevents from 1945 LST on March 25, 2022, to 0615 LST on March 26, 2022: (case 1), and
 293 2100 LST on September 5, 2022, to 0300 LST on September 65, 2022 (case 2), Fig. 56 illustrates the hyetographs of the
 294 rainfall event considered in this study according to the time resolution. The total rainfall of case 1 and 2 is 18.619.5 and 48.7
 295 mm based on the PARSIVEL-, respectively. The maximum rain rate is 9.910.0 and 20.7 mm h⁻¹ based on the 1 min resolution,
 296 and 1.15.0 and 14.5 mm h⁻¹ based on the 15 min resolution for case 1 and case 2.

서식 있음: 위치: 가로: 왼쪽, 기준: 세로 막대형, 세로: 기본, 기준: 여백, 가로: 0 글자, 텍스트 배치: 둘러싸기

서식 있음: 위치: 가로: 왼쪽, 기준: 세로 막대형, 세로: 기본, 기준: 여백, 가로: 0 글자, 텍스트 배치: 둘러싸기

서식 있음: 위치: 가로: 왼쪽, 기준: 세로 막대형, 세로: 기본, 기준: 여백, 가로: 0 글자, 텍스트 배치: 둘러싸기

서식 있음: 위치: 가로: 왼쪽, 기준: 세로 막대형, 세로: 기본, 기준: 여백, 가로: 0 글자, 텍스트 배치: 둘러싸기

서식 있음: 위치: 가로: 왼쪽, 기준: 세로 막대형, 세로: 기본, 기준: 여백, 가로: 0 글자, 텍스트 배치: 둘러싸기

서식 있음: 위치: 가로: 왼쪽, 기준: 세로 막대형, 세로: 기본, 기준: 여백, 가로: 0 글자, 텍스트 배치: 둘러싸기

서식 있음: 위치: 가로: 왼쪽, 기준: 세로 막대형, 세로: 기본, 기준: 여백, 가로: 0 글자, 텍스트 배치: 둘러싸기

서식 있음: 위치: 가로: 왼쪽, 기준: 세로 막대형, 세로: 기본, 기준: 여백, 가로: 0 글자, 텍스트 배치: 둘러싸기

서식 있음: 위치: 가로: 왼쪽, 기준: 세로 막대형, 세로: 기본, 기준: 여백, 가로: 0 글자, 텍스트 배치: 둘러싸기

서식 있음: 위치: 가로: 왼쪽, 기준: 세로 막대형, 세로: 기본, 기준: 여백, 가로: 0 글자, 텍스트 배치: 둘러싸기

서식 있음: 위치: 가로: 왼쪽, 기준: 세로 막대형, 세로: 기본, 기준: 여백, 가로: 0 글자, 텍스트 배치: 둘러싸기

서식 있음: 위치: 가로: 왼쪽, 기준: 세로 막대형, 세로: 기본, 기준: 여백, 가로: 0 글자, 텍스트 배치: 둘러싸기

서식 있음: 위치: 가로: 왼쪽, 기준: 세로 막대형, 세로: 기본, 기준: 여백, 가로: 0 글자, 텍스트 배치: 둘러싸기

서식 있음: 위치: 가로: 왼쪽, 기준: 세로 막대형, 세로: 기본, 기준: 여백, 가로: 0 글자, 텍스트 배치: 둘러싸기

서식 있음: 위치: 가로: 왼쪽, 기준: 세로 막대형, 세로: 기본, 기준: 여백, 가로: 0 글자, 텍스트 배치: 둘러싸기

서식 있음: 위치: 가로: 왼쪽, 기준: 세로 막대형, 세로: 기본, 기준: 여백, 가로: 0 글자, 텍스트 배치: 둘러싸기

서식 있음: 줄 간격: 1줄

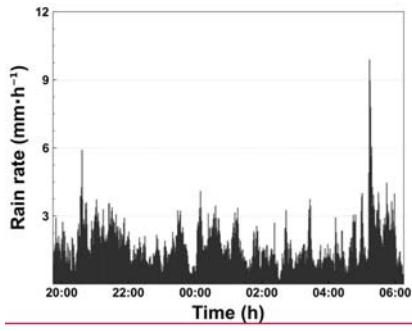
서식 있음: 줄 간격: 1줄

서식 있음: 줄 간격: 1줄

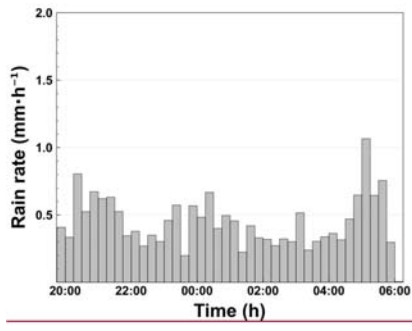
서식 있음: 줄 간격: 1줄

서식 있음: 줄 간격: 1줄

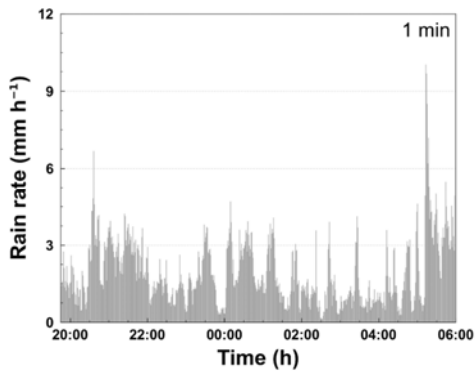
서식 있음: 줄 간격: 1줄



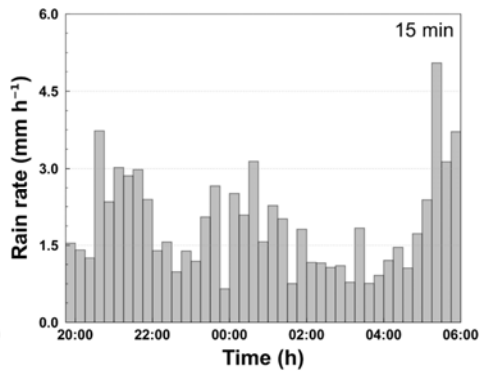
(a) 1 min

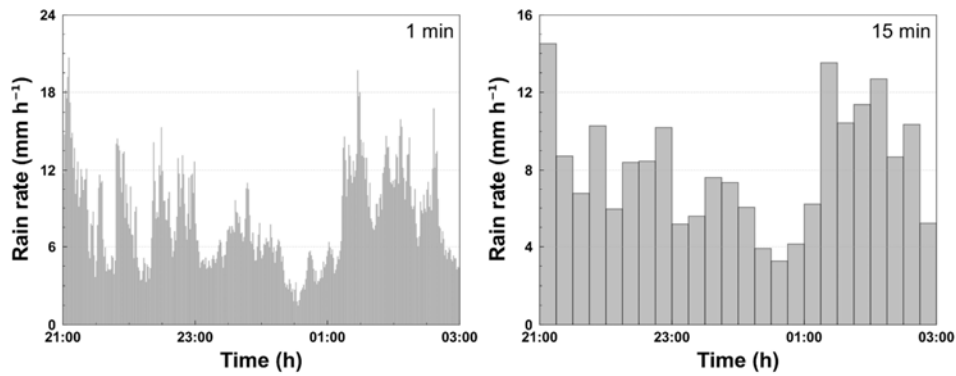


(b) 15 min



(a) Case 1





(b) Case 2

298 Figure 56: Hyetograph of PARSIVEL and rain gauge observation data for the rainfall events considered in this study (left: 1
299 min resolution, right: 10 min resolution).

300
301 In order to secure the quantitative reliability of the PARSIVEL observation data, rain gauge observation data were used to
302 verify the rainfall calculated through the PARSIVEL observation. The rainfall data used for verification are rain gauge
303 observation data operated by KMA (Korea Meteorological Administration) installed closer than 4 km from the PARSIVEL
304 observation site (Table 3). The rainfall comparison period is from September 14, 2021, to October 4, 2022, including the period
305 of the analysis case. Fig. 7 shows scatter plots comparing hourly rain rates from rain gauges and PARSIVEL. As a result of
306 comparison with the observation data at three rain gauge sites, it had low MAE (Mean Absolute Error), RMSE (Root Mean
307 Square Error), MAPE (Mean Absolute Percent Error) values of less than 0.11 mm h⁻¹, 0.6 mm h⁻¹, and 8%. Also, correlation
308 values were more than 0.9.

309 Table 3. Location information of rain gauge observation sites.

Raingague site	Latitude (°)	Longitude (°)	Range from PARSIVEL site (km)
G1	37.4933	126.9175	3.73
G2	37.5196	126.9763	2.42
G3	37.5249	126.9390	2.87

서식 있음: 들여쓰기: 첫 줄: 1.42 글자

서식 있음: 글꼴 색: 자동

서식 있음: 글꼴 색: 자동, 위 첨자

서식 있음: 글꼴 색: 자동

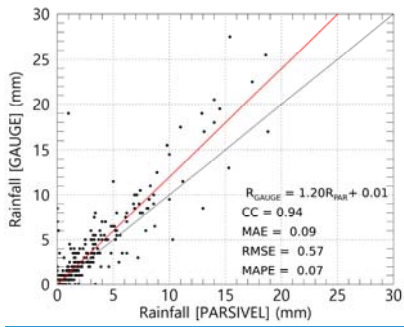
서식 있음: 글꼴 색: 자동

서식 있음: 글꼴 색: 자동

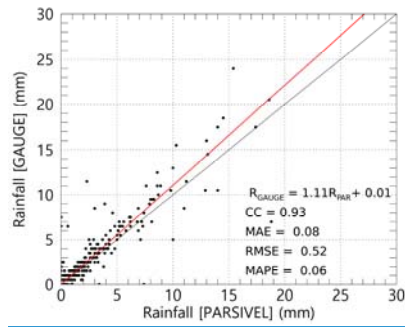
서식 있음: 글꼴 색: 자동

서식 있음: 글꼴 색: 자동

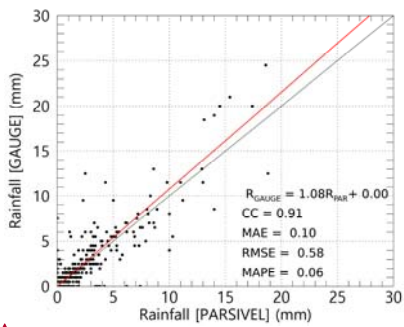
310



(a) G1



(b) G2



(a) G3

저식 있음: 글꼴 색: 자동

저식 있음: 글꼴 색: 자동

저식 있음: 글꼴 색: 자동

저식 있음: 글꼴 색: 자동

저식 있음: 글꼴 색: 자동

311 **Figure 7. Scatter plot of rainfall amount every 1 hour from the PARSIVEL observation and the rain gauge observation.**

312 **4.2 Identifying rainfall streaks**

313 The rain streaks were distinguished from the original raw images using the KNN-based algorithm described in Section 2.4.2.
 314 Accordingly, two parameters (history and dist2Threshold) were set to default values (500 and 400). The other parameter
 315 (detectShadows) was set to “false.” Fig. 6.78 illustrates the raw, background, and rain streaks images for an example time
 316 image (20:30:57 March 25, 2022), scaled in yellow to make it easier to verify the visual change.



(a) Raw image (b) Background image (c) Rain streaks image

서식 있음: 글꼴: 10 pt

317 Figure 678: Segmentation example of raw image into background and rain streaks image based on KNN-based algorithm (20:30:57
318 March 25, 2022).

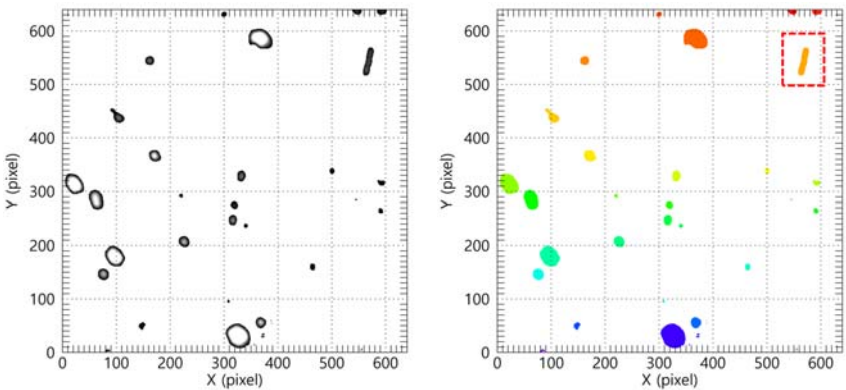
319 As confirmed in Fig. 678, adequate background separation performance can be achieved using the KNN-based method
320 used in this study. Because it is an infrared camera and the camera's exposure time is 1/250 s, the length of rain streaks is
321 relatively short. The longer the exposure time, the longer the raindrops appear on the image (Schmidt et al., 2012; Allamano
322 et al., 2015). If the exposure time is too long, some rain streaks may penetrate the image. In this case, it is difficult to estimate
323 the rain streak length, a clue for estimating raindrop size.

324 The identification algorithm was implemented using Anaconda Software Distribution on a workstation with an AMD Ryzen
325 5 5600X 6-Core Processor and 32 GB RAM. The computing time for the 15 min video was approximately 50 s using only
326 CPU computation. As described previously, the KNN-based algorithm used in this study has high-speed computing
327 performance compared with various algorithms based on optimization, so it will likely have an advantage in real-time
328 applications.

329 4.3 Estimation of DSD and rain rate

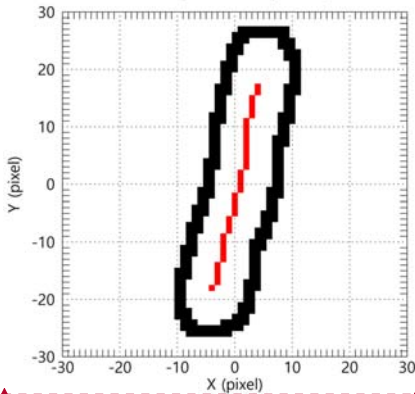
330 The rain streaks image presented in Fig. 687(c) was not considered for the final DSD estimation because of noise and factors
331 other than rain caused by the sudden brightness change. As described in Section 3, a low-pass filter was first applied rain
332 streaks image.

333 The 10×10 kernel was applied considering the total image size (640×640), and each grid value of the kernel was set to
334 0.01. The set kernel was filtered by convolution pixel by pixel. Moreover, the convolution was performed once more using the
335 following 2D kernel $\begin{bmatrix} 0 & 1 & 0 \\ -1 & 0 & 1 \\ 0 & -1 & 0 \end{bmatrix}$ to highlight the rim of the rain streaks. A background layer with a value of 0 and a
336 part not in the image were separated to extract the rain streaks, which were labeled one by one to identify each rain streak from
337 the image. Fig. 789(a) illustrates the example result after performing the processes described above to Fig. 678(c). Each rain
338 streak was then separated and labeled, as in Fig. 789(b).

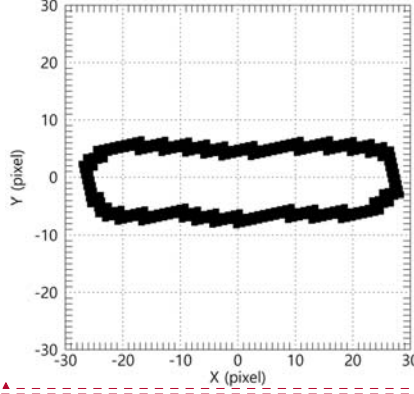


(a) Rain streaks image refined by low-pass filter

(b) Separated and labeled rain streaks



(c) Center axis for a rain streak



(d) Rotated rain streak considering canting angle

339 **Figure 789.** Extraction example of rain streak based on the proposed algorithm.

340 The border information of each rain streak needed to be obtained. The center axis was calculated by connecting the center
 341 (median) of the minimum pixel and maximum pixel values of the x-axis for each y-axis using border information. The angle
 342 of rain streak was obtained from the slope value obtained by calculating the linear function through the center axis's x and y
 343 pixel number values. Fig. 789(c) is an example of the extraction of a rain streak extracted from the image of Fig. 789(b).

344 The drop angle was then calculated, and the rain streak was rotated using the angle information. Raindrops can be broken
 345 up by strong wind or collisions between raindrops during falling. The maximum difference value between the minimum and
 346 maximum pixel number values of y-axis calculated using border information of the rotated rain streak was used to calculate the
 347 raindrop diameter and exclude the influence of the distorted shape of rain streak by break up (Fig. 789(d)) (Testik, 2009;

서식 있음: 글꼴: 1줄

서식 있음: 글꼴: 10 pt

서식 있음: 글꼴: 1줄

서식 있음: 글꼴: 10 pt

서식 있음: 글꼴: 1줄

서식 있음: 글꼴: 10 pt

서식 있음: 글꼴: 10 pt

서식 있음: 글꼴: 10 pt

서식 있음: 글꼴: 1줄

348 Testik and Pei, 2017). Fig. 789(d) illustrates the result of the final process. If the rain streaks overlap, the diameter of the
349 raindrops can be estimated as large. To reduce the overestimation of raindrop diameter, this study tried to find the main central
350 axis coordinates of overlapping rain streaks and set the longest central axis as the representative value. Then, estimate the
351 primary diameter by calculating the distance between each pixel value of the set central axis and the edge pixels of rain streaks.

352 Fig. 8910 illustrates the time series of the number concentration and D_m obtained from CCTV and PARSIVEL. From 1945
353 LST to 2350 LST, the maximum number concentration of lower than $1,000 \text{ mm}^{-1}\text{m}^{-3}$ was observed from the PARSIVEL
354 observation, and from 2000 LST to 2010 LST, a number concentration lower than $100 \text{ mm}^{-1}\text{m}^{-3}$ was observed. At 2005 LST,
355 large raindrops (of 3.8 mm) were observed, resulting in a sharp increase in D_m above 2 mm. In contrast, in the results based on
356 CCTV images, the number concentration of less than $10,000 \text{ mm}^{-1}\text{m}^{-3}$ was continuously demonstrated during the entire analysis
357 period, and a number concentration greater than $5,000 \text{ mm}^{-1}\text{m}^{-3}$ was observed before 2200 LST. Because the proportion of
358 small drops was high, D_m was predominantly less than 1.5 mm.

359 From 0000 LST to 0100 LST, both CCTV and PARSIVEL-based data had a predominant maximum diameter of about 2.4
360 mm. At 0035 LST, raindrops larger than 3.2 mm were observed in PARSIVEL, but raindrops less than 3 mm were not observed
361 in CCTV. However, the number concentration of small diameters of 0.5 mm or less had similar values between 1,000 and
362 $5,000 \text{ mm}^{-1}\text{m}^{-3}$. Despite the difference in the maximum size of the drops, there was no predominant difference in the D_m
363 because the number concentration of raindrops smaller than 1 mm had similar values.

364 From 0300 LST to 0530 LST, number concentrations higher than $5,000 \text{ mm}^{-1}\text{m}^{-3}$ in the raindrops smaller than 1 mm were
365 observed using PARSIVEL. However, CCTV data revealed that number concentrations less than $5,000 \text{ mm}^{-1}\text{m}^{-3}$ were
366 consistently observed. ~~At 1714 From 0500 LST, raindrops of up to 3.2 mm were observed through PARSIVEL, but the~~
367 ~~maximum diameter was overestimated to be greater than 3.5 mm~~ 0510 LST, CCTV image-based on CCTV. In CCTV images,
368 the D_m was close to 3 mm because of the overestimation of diameter and underestimation of number concentration consistently
369 appeared as about 1.2 mm, whereas D_m was smaller than 0.7 mm in PARSIVEL. The cause for raindrops less than 1 mm.
370 ~~There the rapid decrease in D_m of the PARSIVEL was that the CCTV-based maximum diameter is about 2.4 mm, which was a~~
371 ~~difference with similar to the D_m value obtained through PARSIVEL observation data, but the number concentration of 0.5 to~~
372 ~~0.6 mm raindrops observed by PARSIVEL had a large value of more than $10,000 \text{ mm}^{-1}\text{m}^{-3}$.~~

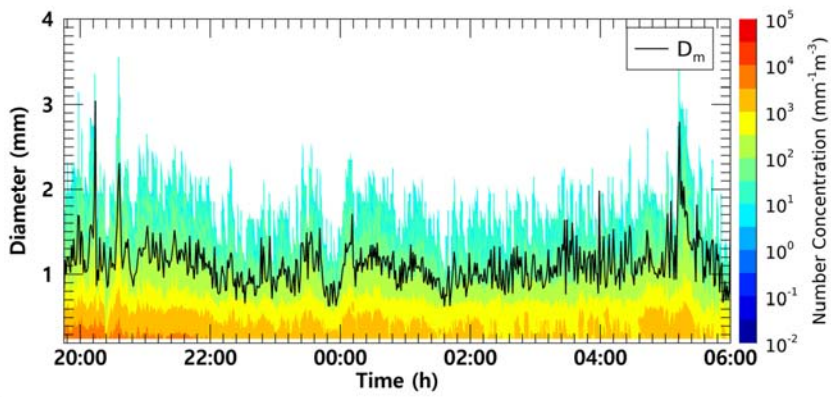
373

서식 있음: 글꼴: 기움임꼴

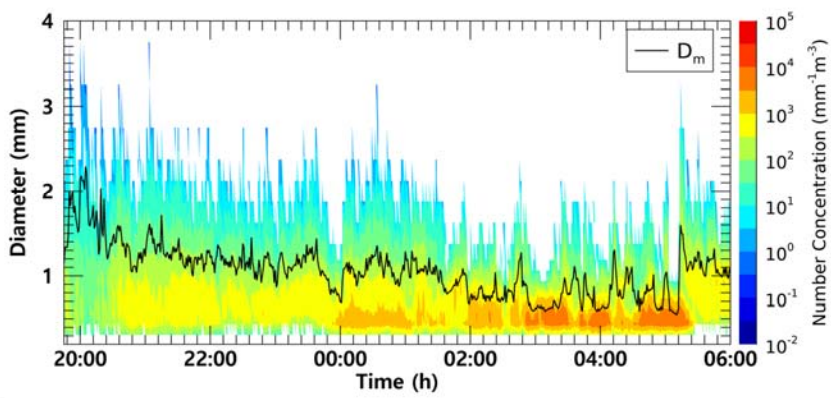
서식 있음: 글꼴: 기움임꼴, 아래 첨자

서식 있음: 글꼴: 기움임꼴

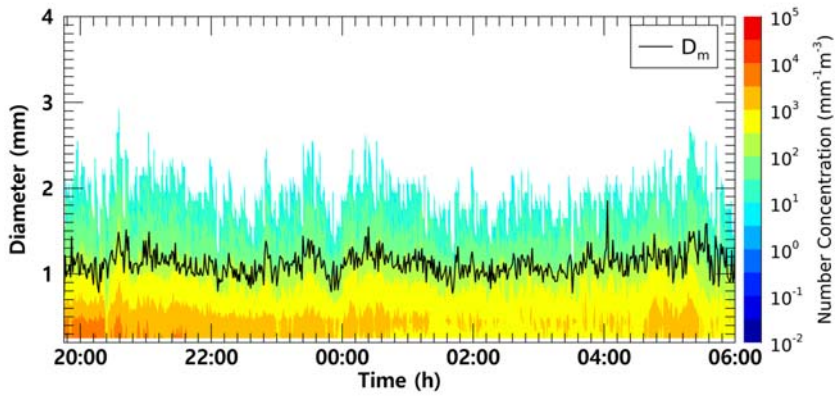
서식 있음: 글꼴: 기움임꼴, 아래 첨자



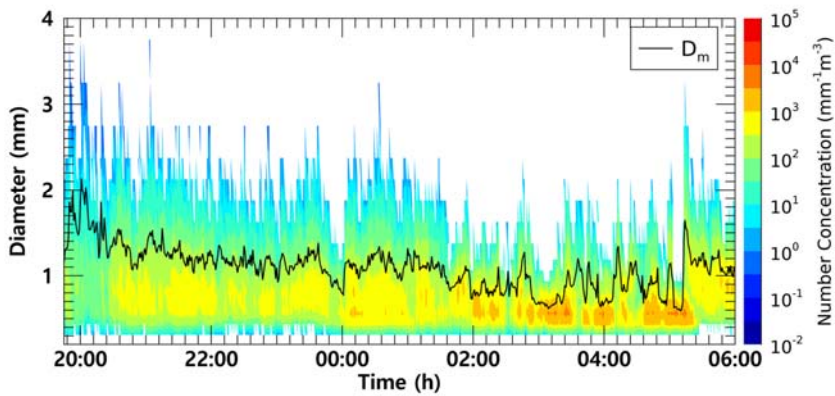
(a) CCTV



374



(a) CCTV



(b) PARSIVEL

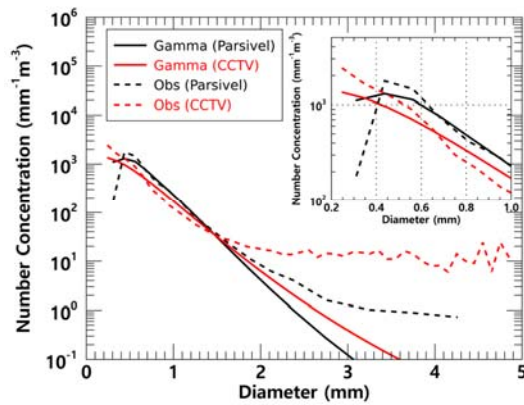
375 Figure 8910.: Time series of number concentration and D_m (black coloured line) from (a) the surveillance camera images, (b) the
 376 PARSIVEL observation data from 2145 LST on March 25 to 0600 LST on March 26, 2022-. (case 1).

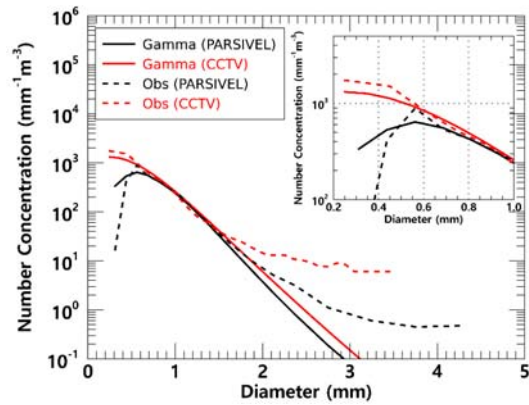
377 Fig. 94011 illustrates the average number concentration versus diameter of raindrops calculated using CCTV image and
 378 PARSIVEL observation data from 1945 LST on March 25 to 0600 LST on March 26, 2022. The PARSIVEL disdrometer data
 379 has a fixed raindrop diameter channel; thus, it can differ in number concentration depending on the diameter channel setting.

서식 있음: 아래 첨자

380 Therefore, in this study, the simulated DSD through the gamma model was also analyzed to compare the distribution of rainfall
381 particles.

382 For raindrop diameters from 0.7 to 1.5 mm, the simulated and observed number concentrations produced similar values.
383 However, above 1.5 mm, the model-based number concentration was under-simulated. From these results, in the precipitation
384 ~~cases~~ selected in this study, the gamma model appears limited in simulating the number concentration of raindrops larger
385 than 3 mm. In diameters from 0.5 to 1.5 mm and above 1.5 mm, the number concentration obtained from CCTV images
386 tended to be ~~lower~~ higher than that from PARSIVEL observation ~~and higher in diameters above 1.5 mm~~. PARSIVEL
387 observation data decreased sharply for diameters smaller than 0.3 mm. In contrast, CCTV gradually increased the number
388 concentration as the diameter decreased.

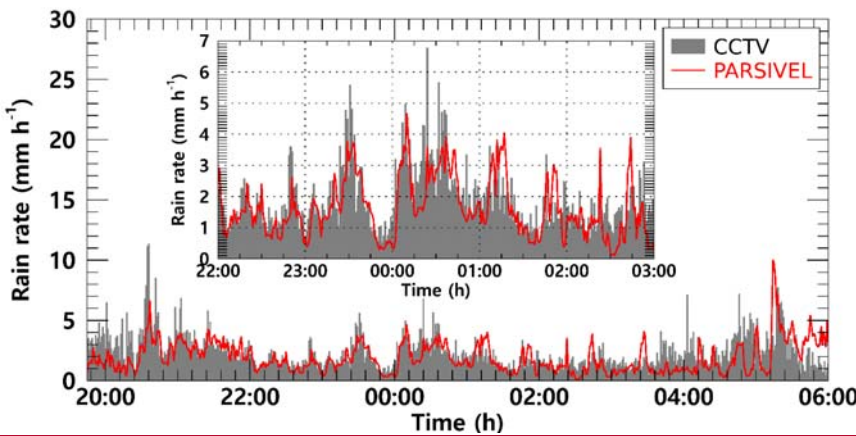
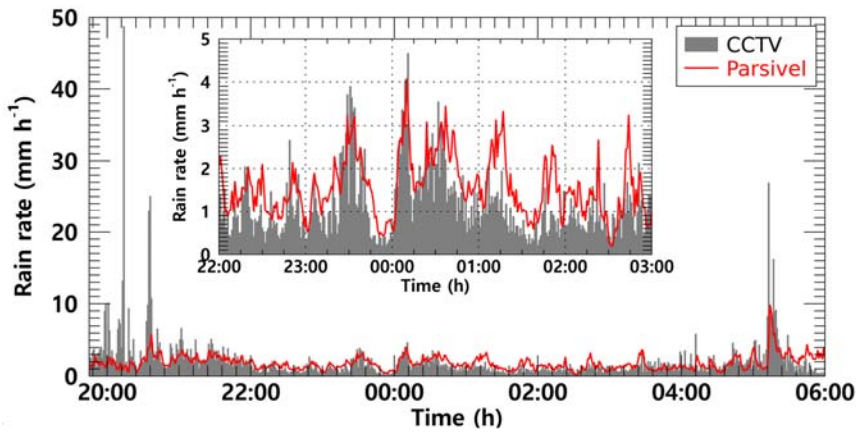




389 Figure 9: Average number concentration versus diameter from the surveillance camera images and the PARSIVEL. (case 1).

390 Rainfall intensity was estimated based on the obtained number concentration from CCTV images and PARSIVEL. The
 391 near (s_n) and far (s_f) focus planes were calculated as 718 and 1,648 mm from Eqs. (8) and (9). The DoF was calculated as 930
 392 mm. The focal distance was set to 1 m, referring to previous studies (Dong et al., 2017; Jiang et al., 2019). The control volume
 393 was 2.9 m³, applying Eq. (10) with the variables determined above. Fig. 10 illustrates the rain rate time series calculated
 394 using CCTV images and PARSIVEL observation data. The increase or decrease in rain rate according to time change based
 395 on CCTV data followed the trend of rainfall intensity change based on PARSIVEL observation data.

396 At 0400 LST and 0516 LST, the PARSIVEL observation data revealed rain rates of up to 1. based rain rate was 5
 397 mm h⁻¹ and 9.8 mm h⁻¹, but the CCTV image-based rain rates were overestimated to be larger than 3.5 higher than 10
 398 mm h⁻¹. On the other hand, the CCTV based rain rate was underestimated by about 2 mm h⁻¹ and 15 mm h⁻¹. During the period
 399 where the difference in rain rate is large, compared with the PARSIVEL observation data, relatively larger-based rain
 400 rate at 0514 LST. Quantitative changes in CCTV based rain rate showed a similar tendency to increase and decrease the number
 401 concentration of raindrops were applied to the rain rate calculation, resulting in an error. At 2014 smaller than 1 mm and the
 402 maximum diameter. From 0100 LST on March 25 and at 0516 to 0200 LST on March 26, raindrops larger than 3.5 mm were
 403 considered in the rain rate calculation, which increased, when the number concentrations of CCTV and PARSIVEL had similar
 404 values, the rain rate error also showed similar results.



405 Figure 4-112: The rain rate time series calculated from the surveillance camera images (gray bar) and PARSIVEL observation
 406 data (red line) from 2145 LST on March 25 to 0600 LST on March 26, 2022. (case 1).

407 Fig. 4-113 illustrates the scatter plot of the average rain rate every 15 min from the PARSIVEL observation and the
 408 CCTV images. Uncertainty exists in the resolution of the rain gauge in the 1 min step. Accordingly, the time step for analysis
 409 is set to 15 min. The slope of the rainfall intensity regression line was close to 1 except for 0.71 because the period when

410 the CCTV based rain rate was overestimated by the raindrops larger than 3 mm. During the entire analysis time,
 411 the rain rate slope was 1.33, revealing that the error increased with rainfall intensity of weaker than 2 mm h⁻¹.

412 The cumulative average rainfall intensity every 15 min was weaker than 10 mm h⁻¹, concentrated at a rain rate less than 46
 413 mm h⁻¹, so the correlation coefficient (CC) was 0.5864. Furthermore, the mean absolute error (MAE), root mean square error
 414 (RMSE), and mean absolute percent error (MAPE) were 0.8461 mm h⁻¹, 1.430.99 mm h⁻¹, and 444.8%. Differences according
 415 to rain rate can also be determined. The accuracy is higher at a rain rate smaller than 2 mm h⁻¹ as a boundary. The MAE, RMSE,
 416 and MAPE were 0.3229 mm h⁻¹, 0.6772 mm h⁻¹, and 323.8% for a rain rate of 2 mm h⁻¹ or less, and 1.490.58 mm h⁻¹, 2.371.17
 417 mm h⁻¹, and 735.5% for a rain rate above 2 mm h⁻¹.

418 The statistical values of the rain rate and DSD parameters for the rainfall cases analyzed in this study are summarized in
 419 Table 53. The rain rate and D_m calculated using CCTV images were 0.16459 mm h⁻¹ and 0.05025 mm more than the values
 420 calculated using PARSIVEL observation data on average, respectively. A high rain rate and D_m were caused by overestimating
 421 the number concentration for raindrops larger than 1.5 mm confirmed in Fig. 910. The number concentration for the small
 422 diameter (less than 0.3 mm) was higher in the CCTV data than in the PARSIVEL data. Due to the high concentration value of
 423 the number concentration of raindrops below 0.5 mm and above 2 mm, the CCTV based rain rate had a large value.

424 However, the rain rate was not significantly affected by small raindrops. Although D_m calculated from the PARSIVEL
 425 observation data had a low value (1.061 mm), the CCTV data revealed a high skewness (of 1.793) because of the high number
 426 concentration for raindrops smaller than 0.1 mm. the high kurtosis (104.945 and 7.849) for the rain rate and D_m of the CCTV-
 427 based data were caused by the overestimated number concentration of 1.5 mm or larger. Moreover, as the distribution spread
 428 widely, μ was as low as 1.312. Because of the high number concentration for raindrops larger than 3 mm of CCTV, the
 429 PARSIVEL observation data had a A value of 9.982 mm⁻², whereas the CCTV data had a low value (5.187 mm⁻²).

430 In the D_m calculated through the PARSIVEL observation data, the concentration change of small drops over time was large,
 431 and the variance (0.063 mm) of D_m was large due to the rapid change in number concentration. The variability of the maximum
 432 diameter was greater in the PARSIVEL observation data, but the variance of the rain rate was greater in the CCTV data. The
 433 large variability of the concentration of raindrops below 3 mm was effected the change in the rain rate. Also, due to the high
 434 number concentration of small drops, the skewness of CCTV (1.903) based rain rate had a higher value than that of the
 435 PARSIVEL (1.589) based rain rate. The low variability (0.063 mm) of the D_m calculated from CCTV data means that the
 436 change in the shape of the raindrop size distribution was small, supported by the low variance of A (3.016 mm⁻¹).

437 Table 53.: Statistical values of the rain rate and DSD parameters for the rainfall case in this study.

		R (mm h ⁻¹)	D_m (mm)	$\text{Log}_{10}N_0$ $\log_{10}N_0$ (mm ⁻³)	μ (unitless)	A A (mm ⁻²)
PARSIVEL	Mean	1.829905	1.06109 1	6.5837.37 9	5.1037.39 4	9.98211.8 29
	Variance	1.013667	0.08806 3	11.76815. 170	24.12435. 975	69.89988. 288

- 서식 있음: 글꼴: 기움입꼴
- 서식 있음: 글꼴: 기움입꼴
- 서식 있음: 간격: 단락 뒤: 0 pt, 줄 간격: 1줄
- 서식 있음: 간격: 단락 뒤: 0 pt, 줄 간격: 1줄
- 서식 있음: 줄 간격: 1줄

CCTV	Skewness	$\frac{2.341158}{9}$	$\frac{0.81455}{1}$	2.447470	2.44015	2.687714
	Kurtosis	$\frac{12.29551}{89}$	$\frac{1.56223}{3}$	7.226751	5.335132	8.549165
	Mean	$\frac{1.994236}{4}$	1.116	4.405857	$\frac{1.312213}{1}$	5.187713
	Variance	$\frac{9.274199}{8}$	0.07021	0.422472	$\frac{0.913168}{0}$	3.527016
	Skewness	$\frac{8.528190}{3}$	$\frac{1.7930}{536}$	1.427109	$\frac{1.075062}{8}$	1.441151
	Kurtosis	$\frac{104.9456}{073}$	$\frac{7.8491}{041}$	2.731188	$\frac{1.664073}{9}$	2.802506

서식 있음: 줄 간격: 1줄

서식 있음: 줄 간격: 1줄

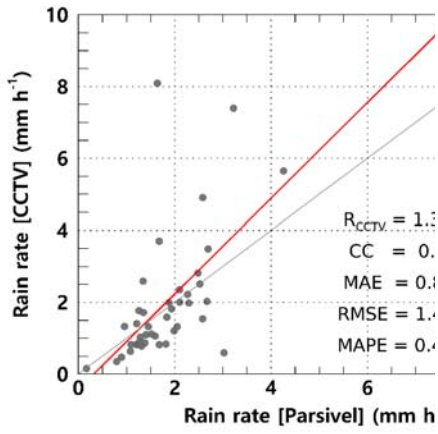
서식 있음: 줄 간격: 1줄

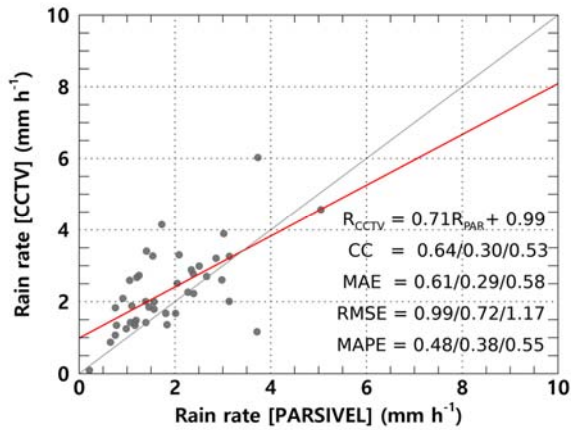
서식 있음: 줄 간격: 1줄

서식 있음: 간격 단락 뒤: 0 pt, 줄 간격: 1줄

서식 있음: 줄 간격: 1줄

서식 있음: 줄 간격: 1줄





439 **Figure. 4-1213.** Scatter plot of average rain rate every 15 minutes from the PARSIVEL observation and the surveillance camera
 440 images. **(case 1).** Red line is linear regression. Scatter plot displays CC, MAE, RMSE, MAPE for $R > 0 \text{ mm h}^{-1}$, $R < 2 \text{ mm h}^{-1}$, and R
 441 $\geq 2 \text{ mm h}^{-1}$ (sequentially from left to right).

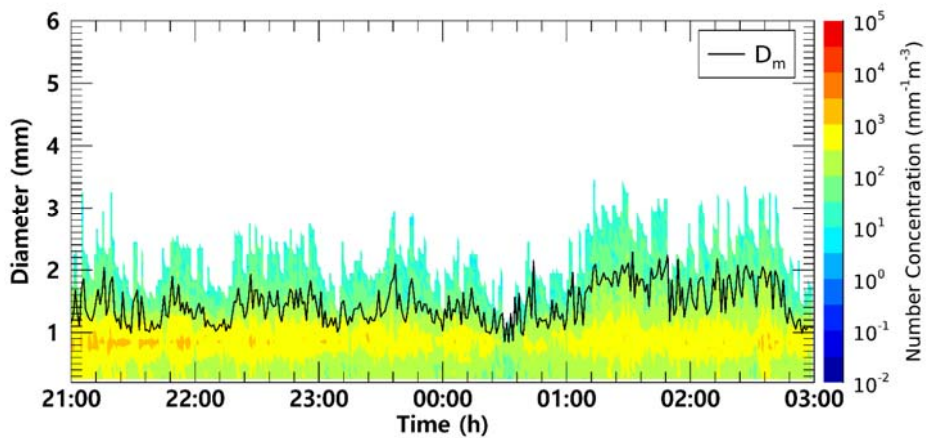
442

← 서식 있음: 캡션

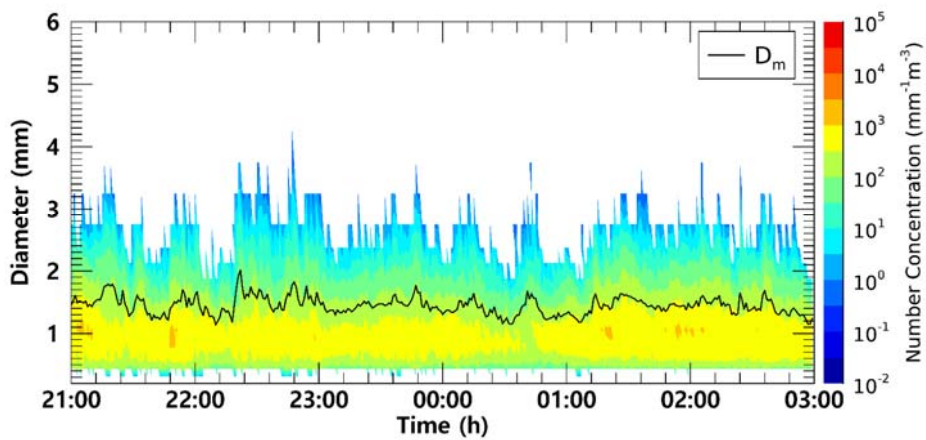
443 Fig. 1314 illustrates the time series of the number concentration and D_m obtained from CCTV and PARSIVEL for case 2.
 444 In both CCTV and PARSIVEL observation data, the number concentration for a diameter between 0.5 mm and 1.5 mm had a
 445 value between $500 \text{ mm}^{-1}\text{m}^{-3}$ to $5,000 \text{ mm}^{-1}\text{m}^{-3}$, and there was no significant change in the number concentration with time.

446 The maximum diameter also consistently had a value close to about 3 mm, and the D_m was also similar to about 1.5 mm
 447 because the maximum diameter and the number concentration of 1 mm intermediate drop had similar values.

448 From 0100 LST to 0230 LST, the maximum particle diameter through CCTV was overestimated, resulting in a large value
 449 close to 3.5 mm. As a result, the D_m value increased significantly to more than 2 mm. PARSIVEL data showed a sharp decrease
 450 in the number concentration of 1 mm drops at 0030 LST, and an increase in D_m under the influence of the decreased number
 451 concentration. However, in the case of CCTV, only raindrops smaller than of 1.5 mm were observed at the time, and there was
 452 similar in that D_m was decrease (about 1.1 mm).



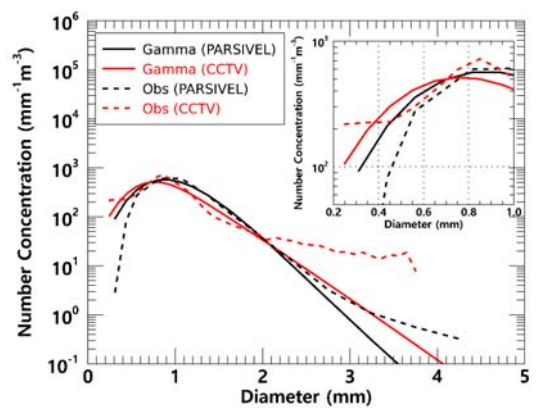
(a) CCTV



(b) PARSIVEL

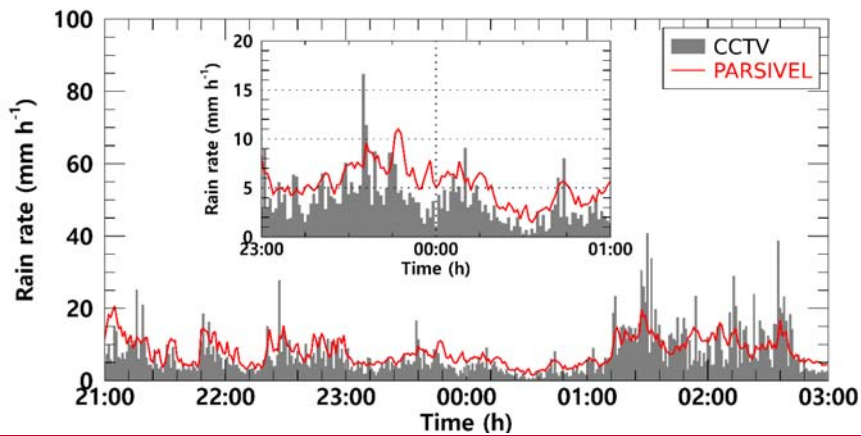
453 Figure 1314.: Time series of number concentration and D_m (black coloured line) from (a) the surveillance camera images, (b) the
 454 PARSIVEL observation data from 2100 LST on September 5 to 0300 LST on September 6, 2022 (case 2).

455 As clearly shown in Fig. 4314, there was no significant difference in number concentration according to the time change.
 456 The average number concentration distribution also showed similar results because the number concentration values were
 457 concentrated at $1,000 \text{ mm}^{-1}\text{m}^{-3}$ concentration in both observation instruments. (Fig. 4415). As in case 1, PARSIVEL
 458 observation data showed a tendency to underestimate in sections less than 0.5 mm and underestimated in sections larger than
 459 2 mm compared to CCTV data. The diameter section where CCTV data is underestimated compared to PARSIVEL data was
 460 from 1 mm to 2 mm. Since the number concentration of the CCTV data was underestimated in this section, the rain rate based
 461 on the number concentration data was also underestimated compared to the rainfall intensity based on the PARSIVEL data.



462 **Figure 4415.: Average number concentration versus diameter from the surveillance camera images and the PARSIVEL (case 2).**

463 Between 2100 LST on September 5 and 0100 LST on September 6, when the number concentration of about 1 mm
 464 raindrops is similar and the maximum diameter size is similar, the rain rate time series distribution has a value of about 5 mm
 465 h^{-1} and has a very similar flow. However, between 0130 LST and 0300 LST, which is a time period with overestimation of
 466 raindrop diameter in CCTV observation data, the increase and decrease in rain rate was similar. However, the magnitude of
 467 the increase and decrease rain rate differed every 15 minutes. During that time, the maximum rain rate was less than 20 mm h^{-1}
 468 in the PARSIVEL observation data, while strong rainfall of 30 mm h^{-1} or more was observed in the CCTV observation data.



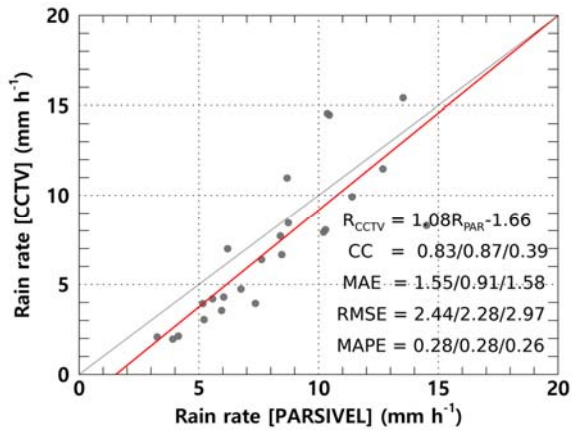
469 **Figure 1615:** The rain rate time series calculated from the surveillance camera images (gray bar) and PARSIVEL observation data
 470 (red line) from 2100 LST on September 5 to 0300 LST on September 6, 2022 (case 2).

471 Fig. 1617 illustrates the scatter plot of the average rain rate every 15 min from the PARSIVEL observation and the CCTV
 472 images for case 2. Compared to case 1, case 2 was a strong rainfall case with a rain rate of about 8.94 mm h⁻¹. Compared to
 473 the PARSIVEL observation data, the CCTV observation data showed a larger D_m by 0.221 mm, while the $\log_{10}N_0$ showed a
 474 small feature of 1.1 mm⁻¹μm⁻³. As the weight of medium and large drops over 1 mm increased, μ and A showed lower values
 475 of 4.262 and 5.397 mm⁻¹, respectively (Table 45). According to the 15-minute cumulative rain rate comparison result, the rain
 476 rate based on CCTV image data tends to be underestimated when it is less than 10 mm h⁻¹. Conversely, there was a tendency
 477 to overestimate the rainfall period of 10 mm h⁻¹ or more. This tendency was confirmed in case 1 which may be caused by
 478 recognizing overlapping rain streaks as a single big raindrop. MAPE had a low value of 0.3% or less regardless of the rain rate,
 479 and even though the rainfall intensity was relatively large compared to case 1. MAE and RMSE did not significantly increase.
 480 This is because there was no abnormally large value of CCTV rainfall during the rainfall period of case 2 compared to case 1.
 481 **Table 45:** Statistical values of the rain rate and DSD parameters for case 2.

서식 있음: 글꼴: 기움임꼴

		R (mm h ⁻¹)	D_m (mm)	$\log_{10}N_0$ (mm ⁻¹ μm ⁻³)	μ (unitless)	A (mm ⁻¹)
PARSIVEL	Mean	8.12	1.445	5.900	6.379	7.341
	Variance	13.82	0.020	1.160	6.498	5.596
	Skewness	0.65	0.447	1.061	0.9467	1.198
	Kurtosis	-0.13	0.472	2.480	1.818	2.792
CCTV	Mean	8.94	1.666	4.813	4.262	5.397
	Variance	69.33	0.121	1.185	4.577	6.714
	Skewness	2.75	0.355	2.596	1.903	2.640
	Kurtosis	11.71	-0.202	8.962	5.714	9.756

482



483 Fig. 4617. Scatter plot of average rain rate every 15 minutes from the PARSIVEL observation and the surveillance camera images
484 (case 2). Red line is linear regression. Scatter plot displays CC, MAE, RMSE, MAPE for $R > 0$ mm h⁻¹, $R < 5$ mm h⁻¹, and $R > 5$
485 mm h⁻¹ (sequentially from left to right).

486 6 Conclusion

487 This study estimated DSD with an infrared surveillance camera, based on which rainfall intensity was also estimated. Rain
488 streaks were extracted using a KNN-based algorithm. The rainfall intensity was estimated based on DSD using physical optics
489 analysis. A rainfall event was selected, and the applicability of the method in this study was examined. The estimated DSD
490 was verified using a PARSIVEL. ~~Furthermore, a tipping bucket rain gauge was used for comparison.~~ The results from this
491 study can be summarized as follows.

492 KNN-based algorithm illustrates suitable performance in separating the rain streaks and background layers. Furthermore,
493 the possibility of separation for each rain streak and estimation of DSD was sufficient.

494 The number concentration of raindrops obtained through the CCTV images was similar to the actual PARSIVEL observed
495 number concentration in the 0.5 to 1.5 mm section. In the small raindrops in the section of 0.4 mm or less, the PARSIVEL
496 observation data underestimates the actual DSD. However, the CCTV image-based rain rate had an advantage over the
497 raindrop-based data—the number concentration decreased rapidly as the number concentration gradually increased in the 0.2–
498 0.3 mm diameter section.

499 The maximum raindrop diameter and number concentration of less than 1 mm produced similar results during the period
 500 with a high ratio of diameters less than 3 mm. However, the number concentration was overestimated during the period when
 501 raindrops larger than 3 mm were observed. The CCTV image-based data revealed that the rain rate was overestimated because
 502 of the overestimation of raindrops larger than 3 mm. After comparing with the 15-min cumulative PARSIVEL rain rate, the
 503 CCs—MAE, RMSE, and MAPE—of case 1 (case 2)—were 0.8461 mm h⁻¹, (1.55 mm h⁻¹), 0.99 mm h⁻¹ (1.43 mm h⁻¹), and
 504 48% (44%,%) . The differences according to rain rate can be identified. The accuracy is higher at a rain rate smaller than 210
 505 mm h⁻¹ as a boundary.

506 The rain rate and D_m calculated using CCTV images exhibited similar average values. The overestimated number
 507 concentration of 1.5 mm or larger caused high kurtosis for the rain rate and D_m of CCTV-based data and a low μ value. Because
 508 of the high number concentration for raindrops larger than 3 mm of CCTV, the PARSIVEL observation data had a higher λ
 509 value than the result based on the CCTV data.

510 In this study, DSD was estimated using an infrared surveillance camera; the rain rate was also estimated. Consequently,
 511 we could confirm the possibility of estimating an image-based DSD and rain rate obtained based on low-cost equipment in
 512 dark conditions. Though, the infrared surveillance camera considered in this study will not be able to replace traditional
 513 observation devices, if future studies can be continued to secure robustness, it will be an excellent complement to the existing
 514 observation system in terms of spatiotemporal resolution and accuracy improvement.

515 **Appendix. The diameter and fall velocity information for each diameter channel class.**

516 **Table 1. The representative diameter and spread for each diameter channel class.**

Class number	Class average (mm)	Class spread (mm)	Class number	Class average (mm)	Class spread in (mm)
<u>1</u>	<u>0.062</u>	<u>0.125</u>	<u>17</u>	<u>3.250</u>	<u>0.500</u>
<u>2</u>	<u>0.187</u>	<u>0.125</u>	<u>18</u>	<u>3.750</u>	<u>0.500</u>
<u>3</u>	<u>0.312</u>	<u>0.125</u>	<u>19</u>	<u>4.250</u>	<u>0.500</u>
<u>4</u>	<u>0.437</u>	<u>0.125</u>	<u>20</u>	<u>4.750</u>	<u>0.500</u>
<u>5</u>	<u>0.562</u>	<u>0.125</u>	<u>21</u>	<u>5.500</u>	<u>1.000</u>
<u>6</u>	<u>0.687</u>	<u>0.125</u>	<u>22</u>	<u>6.500</u>	<u>1.000</u>
<u>7</u>	<u>0.812</u>	<u>0.125</u>	<u>23</u>	<u>7.500</u>	<u>1.000</u>
<u>8</u>	<u>0.937</u>	<u>0.125</u>	<u>24</u>	<u>8.500</u>	<u>1.000</u>
<u>9</u>	<u>1.062</u>	<u>0.125</u>	<u>25</u>	<u>9.500</u>	<u>1.000</u>
<u>10</u>	<u>1.187</u>	<u>0.125</u>	<u>26</u>	<u>11.000</u>	<u>2.000</u>
<u>11</u>	<u>1.375</u>	<u>0.250</u>	<u>27</u>	<u>13.000</u>	<u>2.000</u>
<u>12</u>	<u>1.625</u>	<u>0.250</u>	<u>28</u>	<u>15.000</u>	<u>2.000</u>
<u>13</u>	<u>1.875</u>	<u>0.250</u>	<u>29</u>	<u>17.000</u>	<u>2.000</u>
<u>14</u>	<u>2.125</u>	<u>0.250</u>	<u>30</u>	<u>19.000</u>	<u>2.000</u>
<u>15</u>	<u>2.375</u>	<u>0.250</u>	<u>31</u>	<u>21.500</u>	<u>3.000</u>

서식 있음: 글꼴: 기울임꼴
 서식 있음: 글꼴: 기울임꼴, 아래 첨자

서식 있음: 위치: 가로: 왼쪽, 기준: 세로 막대형, 세로: 기본, 기준: 여백, 가로: 0 글자, 텍스트 배치: 둘러싸기

서식 있음: 위치: 가로: 왼쪽, 기준: 세로 막대형, 세로: 기본, 기준: 여백, 가로: 0 글자, 텍스트 배치: 둘러싸기

서식 있음: 위치: 가로: 왼쪽, 기준: 세로 막대형, 세로: 기본, 기준: 여백, 가로: 0 글자, 텍스트 배치: 둘러싸기

서식 있음: 위치: 가로: 왼쪽, 기준: 세로 막대형, 세로: 기본, 기준: 여백, 가로: 0 글자, 텍스트 배치: 둘러싸기

서식 있음: 위치: 가로: 왼쪽, 기준: 세로 막대형, 세로: 기본, 기준: 여백, 가로: 0 글자, 텍스트 배치: 둘러싸기

서식 있음: 위치: 가로: 왼쪽, 기준: 세로 막대형, 세로: 기본, 기준: 여백, 가로: 0 글자, 텍스트 배치: 둘러싸기

서식 있음: 위치: 가로: 왼쪽, 기준: 세로 막대형, 세로: 기본, 기준: 여백, 가로: 0 글자, 텍스트 배치: 둘러싸기

서식 있음: 위치: 가로: 왼쪽, 기준: 세로 막대형, 세로: 기본, 기준: 여백, 가로: 0 글자, 텍스트 배치: 둘러싸기

서식 있음: 위치: 가로: 왼쪽, 기준: 세로 막대형, 세로: 기본, 기준: 여백, 가로: 0 글자, 텍스트 배치: 둘러싸기

서식 있음: 위치: 가로: 왼쪽, 기준: 세로 막대형, 세로: 기본, 기준: 여백, 가로: 0 글자, 텍스트 배치: 둘러싸기

서식 있음: 위치: 가로: 왼쪽, 기준: 세로 막대형, 세로: 기본, 기준: 여백, 가로: 0 글자, 텍스트 배치: 둘러싸기

서식 있음: 위치: 가로: 왼쪽, 기준: 세로 막대형, 세로: 기본, 기준: 여백, 가로: 0 글자, 텍스트 배치: 둘러싸기

서식 있음: 위치: 가로: 왼쪽, 기준: 세로 막대형, 세로: 기본, 기준: 여백, 가로: 0 글자, 텍스트 배치: 둘러싸기

서식 있음: 위치: 가로: 왼쪽, 기준: 세로 막대형, 세로: 기본, 기준: 여백, 가로: 0 글자, 텍스트 배치: 둘러싸기

서식 있음: 위치: 가로: 왼쪽, 기준: 세로 막대형, 세로: 기본, 기준: 여백, 가로: 0 글자, 텍스트 배치: 둘러싸기

서식 있음: 위치: 가로: 왼쪽, 기준: 세로 막대형, 세로: 기본, 기준: 여백, 가로: 0 글자, 텍스트 배치: 둘러싸기

517 **Table 2.** The representative fall velocity and spread for each diameter channel class.

Class number	Class average (m s ⁻¹)	Class spread (m s ⁻¹)	Class number	Class average (m s ⁻¹)	Class spread (m s ⁻¹)
1	0.050	0.100	17	2.600	0.400
2	0.150	0.100	18	3.000	0.400
3	0.250	0.100	19	3.400	0.400
4	0.350	0.100	20	3.800	0.400
5	0.450	0.100	21	4.400	0.800
6	0.550	0.100	22	5.200	0.800
7	0.650	0.100	23	6.000	0.800
8	0.750	0.100	24	6.800	0.800
9	0.850	0.100	25	7.600	0.800
10	0.950	0.100	26	8.800	1.600
11	1.100	0.200	27	10.400	1.600
12	1.300	0.200	28	12.000	1.600
13	1.500	0.200	29	13.600	1.600
14	1.700	0.200	30	15.200	1.600
15	1.900	0.200	31	17.600	3.200
16	2.200	0.400	32	20.800	3.200

518 **Data availability**

519 The data and code can be provided by the corresponding author (hjkim22@cau.ac.kr) upon request. The raw videos and data
520 used in the analysis can be downloaded from <https://doi.org/10.6084/m9.figshare.c.6392430.v1>, and the sample codes are
521 available in a public GitHub repository from https://github.com/jinwook213/Rain_CCTV.git.

522 **Acknowledgements**

523 This research was supported by the Korea Meteorological Administration Research and Development Program (KMI2022-
524 01910) and Basic Science Research Program through the National Research Foundation of Korea (NRF) funded by the
525 Ministry of Education (2022R1I1A1A01065554).

526 - This research was supported by the Chung-Ang University Graduate Research Scholarship in 2021.

527 **References**

528 Allamano, P., Croci, A., Laio, F.: Toward the camera rain gauge. Water Resour. Res. 51 (3), 1744-1757, 2015

서식 있음: 위치: 가로: 왼쪽, 기준: 세로 막대형, 세로: 기본, 기준: 여백, 가로: 0 글자, 텍스트 배치: 둘러싸기

서식 있음: 위치: 가로: 왼쪽, 기준: 세로 막대형, 세로: 기본, 기준: 여백, 가로: 0 글자, 텍스트 배치: 둘러싸기

서식 있음: 위치: 가로: 왼쪽, 기준: 세로 막대형, 세로: 기본, 기준: 여백, 가로: 0 글자, 텍스트 배치: 둘러싸기

서식 있음: 위치: 가로: 왼쪽, 기준: 세로 막대형, 세로: 기본, 기준: 여백, 가로: 0 글자, 텍스트 배치: 둘러싸기

서식 있음: 위치: 가로: 왼쪽, 기준: 세로 막대형, 세로: 기본, 기준: 여백, 가로: 0 글자, 텍스트 배치: 둘러싸기

서식 있음: 위치: 가로: 왼쪽, 기준: 세로 막대형, 세로: 기본, 기준: 여백, 가로: 0 글자, 텍스트 배치: 둘러싸기

서식 있음: 위치: 가로: 왼쪽, 기준: 세로 막대형, 세로: 기본, 기준: 여백, 가로: 0 글자, 텍스트 배치: 둘러싸기

서식 있음: 위치: 가로: 왼쪽, 기준: 세로 막대형, 세로: 기본, 기준: 여백, 가로: 0 글자, 텍스트 배치: 둘러싸기

서식 있음: 위치: 가로: 왼쪽, 기준: 세로 막대형, 세로: 기본, 기준: 여백, 가로: 0 글자, 텍스트 배치: 둘러싸기

서식 있음: 위치: 가로: 왼쪽, 기준: 세로 막대형, 세로: 기본, 기준: 여백, 가로: 0 글자, 텍스트 배치: 둘러싸기

서식 있음: 위치: 가로: 왼쪽, 기준: 세로 막대형, 세로: 기본, 기준: 여백, 가로: 0 글자, 텍스트 배치: 둘러싸기

서식 있음: 위치: 가로: 왼쪽, 기준: 세로 막대형, 세로: 기본, 기준: 여백, 가로: 0 글자, 텍스트 배치: 둘러싸기

서식 있음: 위치: 가로: 왼쪽, 기준: 세로 막대형, 세로: 기본, 기준: 여백, 가로: 0 글자, 텍스트 배치: 둘러싸기

서식 있음: 위치: 가로: 왼쪽, 기준: 세로 막대형, 세로: 기본, 기준: 여백, 가로: 0 글자, 텍스트 배치: 둘러싸기

서식 있음: 위치: 가로: 왼쪽, 기준: 세로 막대형, 세로: 기본, 기준: 여백, 가로: 0 글자, 텍스트 배치: 둘러싸기

서식 있음: 위치: 가로: 왼쪽, 기준: 세로 막대형, 세로: 기본, 기준: 여백, 가로: 0 글자, 텍스트 배치: 둘러싸기

서식 있음: 위치: 가로: 왼쪽, 기준: 세로 막대형, 세로: 기본, 기준: 여백, 가로: 0 글자, 텍스트 배치: 둘러싸기

529 Atlas, D., Srivastava, R. C., Sekhon, R. S.: Doppler radar characteristics of precipitation at vertical incidence. *Rev. Geophys.*
530 11 (1), 1–35, 1973.

531 Avanzato, R., Beritelli, F.: A cnn-based differential image processing approach for rainfall classification. *Adv. Sci. Technol.*
532 *Eng. Syst. J.* 5 (4), 438-444, 2020.

533 Bouwmans, T., El Baf, F., Vachon, B.: Statistical background modeling for foreground detection: A survey. In: Chen, C. H.
534 (Ed.) *Handbook of pattern recognition and computer vision*, fourth ed. World Scientific, Singapore, pp. 181-199, 2010

535 Cai, F., Lu, W., Shi, W., He, S.: A mobile device-based imaging spectrometer for environmental monitoring by attaching a
536 lightweight small module to a commercial digital camera. *Sci. Rep.* 7 (1), 1-9, 2017.

537 [Colli, M., Lanza, L. G., La Barbera, P., Chan, P. W.: Measurement accuracy of weighing and tipping-bucket rainfall intensity](#)
538 [gauges under dynamic laboratory testing. *Atmos. Res.*, 144, 186-194, 2014.](#)

539 Deng, L. J., Huang, T. Z., Zhao, X. L., Jiang, T. X.: A directional global sparse model for single image rain removal. *Appl.*
540 *Math. Model.* 59, 662-679, 2018.

541 Dong, R., Liao, J., Li, B., Zhou, H., Crookes, D.: Measurements of rainfall rates from videos. In 2017 10th International
542 Congress on Image and Signal Processing, BioMedical Engineering and Informatics, IEEE, Shanghai, China, 14-16 October,
543 pp. 1-9, 2017.

544 Duthon, P., Bernardin, F., Chausse, F., Colomb, M.: Benchmark for the robustness of image features in rainy conditions. *Mach.*
545 *Vis. Appl.* 29 (5), 915-927, 2018.

546 Famiglietti, J. S., Cazenave, A., Eicker, A., Reager, J. T., Rodell, M., Velicogna, I.: Satellites provide the big picture. *Sci.* 349
547 (6249), 684-685, 2015.

548 Friedrich, K., Kalina, E. A., Masters, F. J., Lopez, C. R.: Drop-size distributions in thunderstorms measured by optical
549 disdrometers during VORTEX2. *Mon. Weather Rev.* 141 (4), 1182-1203, 2013.

550 Garg, K., Nayar, S. K.: Vision and rain. *Int. J. Comput. Vis.* 75 (1), 3-27, 2007.

551 Guo, B., Han, Q., Chen, H., Shanguan, L., Zhou, Z., Yu, Z.: The emergence of visual crowdsensing: Challenges and
552 opportunities. *IEEE Commun. Surv. Tutor.* 19 (4), 2526-2543, 2017.

553 Guo, H., Huang, H., Sun, Y. E., Zhang, Y., Chen, S., Huang, L.: Chacac: Real-time and fine-grained rain detection and
554 measurement using smartphones. *IEEE Internet Things J.* 6 (1), 997-1009, 2019

555 Haberlandt, U., Sester, M.: Areal rainfall estimation using moving cars as rain gauges-A modelling study. *Hydrol. Earth Syst.*
556 *Sci.* 14 (7), 1139-1151, 2010.

557 Hua, X. S.: The city brain: Towards real-time search for the real-world. In The 41st International ACM SIGIR Conference on
558 Research & Development in Information Retrieval, New York, NY, 8-12 July. pp. 1343-1344, 2018

559 Jiang, S., Babovic, V., Zheng, Y., Xiong, J.: Advancing opportunistic sensing in hydrology: A novel approach to measuring
560 rainfall with ordinary surveillance cameras. *Water Resour. Res.* 55 (4), 3004-3027, 2019.

561 Jiang, T. X., Huang, T. Z., Zhao, X. L., Deng, L. J., Wang, Y.: Fastderain: A novel video rain streak removal method using
562 directional gradient priors. *IEEE Trans. Image Process.* 28 (4), 2089-2102, 2018.

563 Kathiravelu, G., Lucke, T., Nichols, P.: Rain drop measurement techniques: A review. *Water*, 8 (1), 29, 2016.

564 Keating, M. P.: *Geometric, physical, and visual optics*, Second ed. Butterworth-Heinemann, Oxford, UK, 2002.

565 Kidd, C., Becker, A., Huffman, G. J., Muller, C. L., Joe, P., Skofronick-Jackson, G., Kirschbaum, D. B.: So, how much of the
566 Earth's surface is covered by rain gauges?. *Bull. Am. Meteorol. Soc.* 98 (1), 69-78, 2017.

567 Kim, J. H., Sim, J. Y., Kim, C. S.: Video deraining and desnowing using temporal correlation and low-rank matrix completion.
568 *IEEE Trans. Image Process.*, 24 (9), 2658-2670, 2015.

569 Li, Y., Tan, R. T., Guo, X., Lu, J., Brown, M. S.: Rain streak removal using layer priors. In 2016 IEEE Conference on Computer
570 Vision and Pattern Recognition, IEEE, Las Vegas, NV, 27-30 June, pp. 2736-2744, 2016.

571 Löffler-Mang, M., Joss, J.: An optical disdrometer for measuring size and velocity of hydrometeors. *J. Atmos. Ocean. Technol.*
572 17 (2), 130-139, 2000.

573 Marshall, J. S., Palmer, W. M.: The distribution of raindrops with size. *J. Meteor.* 5, 165-166, 1948.

574 McCabe, M. F., Rodell, M., Alsdorf, D. E., Miralles, D. G., Uijlenhoet, R., Wagner, W., Lucieer, A., Houborg, R., Verhoest,
575 N. E. C., Franz, T. E., Shi, J., Gao, H., Wood, E. F.: The future of earth observation in hydrology. *Hydrol. Earth Syst. Sci.* 21
576 (7), 3879-3914, 2017.

577 Michaelides, S., Levizzani, V., Anagnostou, E., Bauer, P., Kasparis, T., Lane, J. E.: Precipitation: Measurement, remote
578 sensing, climatology and modeling. *Atmos. Res.* 94 (4), 512-533, 2009.

579 Nemeth, K., Hahn, J. M.: Enhanced precipitation identifier and new generation of present weather sensor by OTT Messtechnik,
580 In WMO/CIMO Technical Conference, Germany, 2005.

581 Nottle, A., Harborne, D., Braines, D., Alzantot, M., Quintana-Amate, S., Tomsett, R., Kaplan, L., Srivastava, M. B.,
582 Chakraborty, S., Preece, A.: Distributed opportunistic sensing and fusion for traffic congestion detection. In 2017 IEEE
583 SmartWorld, Ubiquitous Intelligence & Computing, Advanced & Trusted Computing, Scalable Computing & Communications,
584 Cloud & Big Data Computing, Internet of People and Smart City Innovation, IEEE, San Francisco, CA, 4-8 August, pp. 1-6,
585 2017.

586 Overeem, A., Leijnse, H., Uijlenhoet, R.: Two and a half years of country-wide rainfall maps using radio links from commercial
587 cellular telecommunication networks. *Water Resour. Res.* 52 (10), 8039-8065, 2016.

588 Qasim, S., Khan, K. N., Yu, M., Khan, M. S.: Performance evaluation of background subtraction techniques for video frames.
589 In 2021 International Conference on Artificial Intelligence, IEEE, Islamabad, Pakistan, 5-7 April, pp. 102-107, 2021.

590 Rabiei, E., Haberlandt, U., Sester, M., Fitzner, D.: Rainfall estimation using moving cars as rain gauges-laboratory
591 experiments. *Hydrol. Earth Syst. Sci.* 17 (11), 4701-4712, 2013.

592 Rabiei, E., Haberlandt, U., Sester, M., Fitzner, D., Wallner, M.: Areal rainfall estimation using moving cars-computer
593 experiments including hydrological modeling. *Hydrol. Earth Syst. Sci.* 20 (9), 3907-3922, 2016.

594 Santhaseelan, V., Asari, V. K.: Utilizing local phase information to remove rain from video. *Int. J. Comput. Vis.*, 112 (1), 71-
595 89, 2015.

596 Schmidt, J. M., Flatau, P. J., Harasti, P. R., Yates, R. D., Littleton, R., Pritchard, M. S., Fischer, J. M., Fischer, E. J., Kohri,
597 W. J., Vetter, J. R., Richman, S., Baranowski, D. B., Anderson, M. J., Fletcher, E., Lando, D. W.: Radar observations of
598 individual rain drops in the free atmosphere. *Proc. Natl. Acad. Sci.* 109 (24), 9293-9298, 2012.

599 Smith, P. L.: Raindrop size distributions: Exponential or gamma—Does the difference matter?. *J. Appl. Meteorol. Climatol.*,
600 42 (7), 1031-1034, 2003.

601 Testik, F. Y.: Outcome regimes of binary raindrop collisions. *Atmos. Res.* 94 (3), 389–399, 2009.

602 Testik, F. Y., Pei, B.: Wind effects on the shape of raindrop size distribution. *J. Hydrometeorol.* 18 (5), 1285-1303, 2017.

603 Tokay, A., Short, D. A.: Evidence from tropical raindrop spectra of the origin of rain from stratiform versus convective clouds.
604 *J. Appl. Meteorol. Climatol.* 35 (3), 355–371, 1996.

605 Tripathi, A. K., Mukhopadhyay, S.: Removal of rain from videos: A review. *Signal Image Video Process.* 8 (8), 1421-1430,
606 2014.

607 Trnovszký, T., Sýkora, P., Hudec, R.: Comparison of background subtraction methods on near infra-red spectrum video
608 sequences. *Procedia Eng.*, 192, 887-892, 2017.

609 Ulbrich, C. W.: Natural variations in the analytical form of the raindrop size distribution. *J. Appl. Meteorol. Climatol.* 22 (10),
610 1764–1775, 1983.

611 Vivekanandan, J., Zhang, G., Brandes, E.: Polarimetric radar estimators based on a constrained gamma drop size distribution
612 model. *J. Appl. Meteorol.* 43 (2), 217-230, 2004.

613 Wang, X., Wang, M., Liu, X., Glade, T., Chen, M., Xie, Y., Yuan, Hao., Chen, Y.: Rainfall observation using surveillance
614 audio. *Appl. Acoust.* 186, 108478, 2022.

615 Yang, P., Ng, T. L.: Gauging through the crowd: A crowd-sourcing approach to urban rainfall measurement and storm water
616 modeling implications. *Water Resour. Res.* 53 (11), 9462-9478, 2017.

617 Yuter, S. E., Houze Jr, R. A.: Measurements of raindrop size distributions over the Pacific warm pool and implications for Z–
618 R relations. *J. Appl. Meteorol.* 36 (7), 847-867, 1997.

619 Zen, R., Arsa, D. M. S., Zhang, R., Er, N. A. S., Bressan, S.: Rainfall estimation from traffic cameras. In: Hartmann, S., Küng,
620 J., Chakravarthy, S., Anderst-Kotsis, G., Tjoa, A., Khalil, I. (Eds.) *Database and Expert Systems Applications*, Springer, Cham,
621 Switzerland, pp. 18-32, 2019.

622 Zivkovic, Z., Van Der Heijden, F.: Efficient adaptive density estimation per image pixel for the task of background subtraction.
623 *Pattern Recognit. Lett.* 27 (7), 773-780, 2006.